

Microscopic origin of quantum supersonic phenomenon in one dimension

Zhe-Hao Zhang,^{1,2} Yuzhu Jiang,^{1,3,*} Hai-Qing Lin,^{4,†} and Xi-Wen Guan^{1,3,4,5,6,‡}

¹*Innovation Academy for Precision Measurement Science and Technology,
Chinese Academy of Sciences, Wuhan 430071, China*

²*University of Chinese Academy of Sciences, Beijing 100049, China*

³*NSFC-SPTP Peng Huanwu Center for Fundamental Theory, Xi'an 710127, China*

⁴*Institute for Advanced Study in Physics and School of Physics Zhejiang University, Hangzhou 310058, China*

⁵*Hefei National Laboratory, Hefei 230088, China*

⁶*Department of Fundamental and Theoretical Physics, Research School of Physics,
Australian National University, Canberra ACT 0200, Australia*

(Dated: June 21, 2024)

Using the Bethe ansatz (BA), we rigorously obtain non-equilibrium dynamics of an impurity with a large initial momentum Q in the one-dimensional (1D) interacting bosonic medium. We show that magnon and exciton-like states obtained from the BA equations drastically determine the oscillation nature of the quantum flutter with the periodicity given by $\tau_{\text{QF}} = 2\pi/(|\varepsilon_c(0)| - |\varepsilon_s(0)|)$. Where the charge and spin dressed energies $\varepsilon_{c,s}(0)$ are precisely given by the thermodynamical BA equations. While we further find a persistent revival dynamics of the impurity with a larger periodicity $\tau_L = L/(v_c(Q - k^*) - v_s(k^*))$ than τ_{QF} , manifesting a quantum reflection induced by the periodic boundary conditions of a finite length L , here $v_{c,s}$ are the sound velocities of charge and spin excitations, respectively, and k^* is a characteristic momentum of the impurity to the Fermi point. Finally, we study the application of such a magnon impurity as a quantum resource for measuring the gravitational force.

Introduction. Quantum many body systems with impurities exhibit rich collective and interference phenomena, ranging from polaron [1–6], to Bogoliubov-Cherenkov radiation [7], shock wave [8–10], Bloch oscillations [11], quantum flutter (QF) [12, 13], etc. When an impurity is injected into a fermionic (or bosonic) medium with a speed larger than the intrinsic sound velocity, the momentum of such an impurity shows a long time oscillation behavior after a fast decay. Such non-equilibrium dynamical phenomenon was named as “quantum flutter” [12, 13], showing quasi-particle behavior of the impurity with transitions between the polaron-like and exciton-like states in the medium of free Fermi gas and the Tonks-Girardeau (TG) Bose gas [5, 6, 13, 14].

Building on advantages of ultracold atoms, quantum simulations of many-body phenomena have been attracted great deal of attention [15–33]. In this scenario, one-dimensional (1D) Bethe ansatz (BA) exactly solvable models of ultracold atoms, laying out profound many-body physics [34–47], provide deep insights into the phenomena of the quasiparticles, such as bosonic and fermionic polarons for the slowly moving impurities [5, 6, 28, 48–54], fractionalized magnon [34, 55] in spin excitations, and supersonic impurity dynamics [12, 13] of the fast moving impurity, etc. Such quasiparticles of polaron, magnon supersonic flutter reveal subtly different collective features emerging in charge, spin and spatiotemporal sectors, respectively, see reviews [56, 57].

On the other hand, the 1D multi-component Bose gases with a spin-independent interaction exhibit a striking feature of ferromagnetism [58, 59]. In this regard, much effort has been devoted to experimentally manipulating spinon and magnon by coupling the ferromagnetic sys-

tems with an optical cavity or external gravitational force [34, 54, 55, 60, 61]. However, a rigorous understanding of the dynamics of such quasiparticles beyond the mean field is still challenging and highly desirable.

In this letter, we report on exact results of QF and quantum revival (QR) of the supersonic impurity injected into a medium of 1D bosonic liquid. Building on the BA of the 1D two-component Bose gas [35, 36], we rigorously calculate the time evolutions of the impurity momentum, momentum distribution and correlation function, allowing us to determine exact microscopic states of QF and revival. We show that the QF is caused essentially by the coherent oscillations between the magnon and exciton-like BA eigenstates, leading to the periodicity given by an exact formula (6). It solely depends on the interaction strength between the particles when the initial velocity of the impurity is greater than the sound velocity of the medium. Whereas the finite-size energies of magnon-like states elegantly determines the QR dynamics with a larger period given by the analytical expression (7), significantly revealing a quantum reflection of excitations with the sound velocities of charge. Finally we further propose a metrological application of a magnon impurity for measuring the gravitational force.

The model and exact solution. We consider the 1D two-component Bose gas described by the Hamiltonian

$$H = \int_0^L dx \left(\frac{\hbar^2}{2m} \sum_{\sigma} \partial \hat{\Psi}_{\sigma}^{\dagger} \partial \hat{\Psi}_{\sigma} + c \sum_{\sigma\sigma'} \hat{\Psi}_{\sigma}^{\dagger} \hat{\Psi}_{\sigma'}^{\dagger} \hat{\Psi}_{\sigma'} \hat{\Psi}_{\sigma} \right), \quad (1)$$

for N bosons of the same mass m with two internal spin states $\sigma = \uparrow, \downarrow$ confined to a 1D system of length L via a δ -function potential. Where $\hat{\Psi}_{\sigma}(x)$ is the field opera-

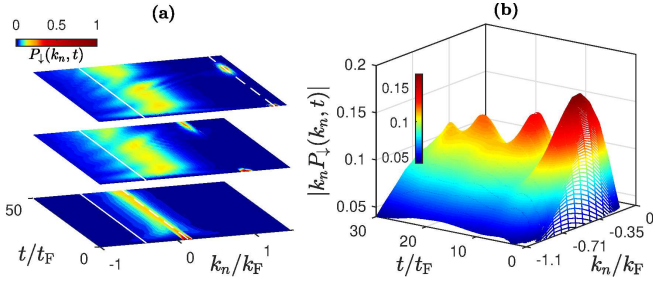


FIG. 1. (a) The time evolution of the impurity momentum distribution P_{\downarrow} for different values of $Q/k_F = 1.33, 1,$ and 0.07 from top to bottom. For $Q \geq k_F$, several persistent peaks occur (white dashed line), showing long time QR at $k_n \approx Q$. When $k_n \approx -0.4k_F$, the undulant behaviour (white solid line) manifests the nature of QF. (b) shows the time evolution of impurity momenta at different k_n s, namely $k_n P_{\downarrow}(k_n, t)$. The undulant peaks near $k_n \approx -0.4k_F$ shows large oscillations of the revival. In both figures we set $\gamma = 10$ and $N = 30$.

tor of the bosons with pseudo-spin σ . The interaction strength $c = -2/a_{1D}$ is tunable via an effective 1D scattering length a_{1D} [62]. We will use the dimensionless interaction strength $\gamma = cL/N$ and set $2m = \hbar = 1$ in our discussions. The model (1) was solved [63] by means of the nested BA [2, 64] for arbitrary M down-spins, also see [59]. Using species selective atomic systems, the related models were studied experimentally on novel quantum impurity dynamics [11, 66, 67].

The eigenfunction of the model (1) can be given by the BA wave function [63] determined by N wave numbers $\{k_i\}$ with $i = 1, \dots, N$ and M spin rapidities $\{\lambda_{\alpha}\}$ with $\alpha = 1, \dots, M$ satisfying the BA equations

$$I_i = \frac{1}{2\pi} k_i L - \frac{1}{2\pi} \sum_{\alpha=1}^M \theta(2k_i - 2\lambda_{\alpha}) + \frac{1}{2\pi} \sum_{j=1}^N \theta(k_i - k_j),$$

$$J_{\alpha} = \frac{1}{2\pi} \sum_{j=1}^N \theta(2\lambda_{\alpha} - 2k_j) - \frac{1}{2\pi} \sum_{\beta=1}^M \theta(\lambda_{\alpha} - \lambda_{\beta}), \quad (2)$$

where $\theta(x) = 2\text{atan}(x/c)$. The quantum numbers are integers or half-integers, $I_j \in \mathbb{Z} + \frac{N-M-1}{2}$, $J_{\alpha} \in \{-\frac{N-M-1}{2}, -\frac{N-M-1}{2} + 1, \dots, \frac{N-M-1}{2}\}$. For a given set of quantum numbers $\{\mathbf{I}_N, \mathbf{J}_M\}$, the Eqs. (2) determine the highest weight and non-highest weight states $|\mathbf{I}_N, \mathbf{J}_M, \ell\rangle = (\hat{S}^-)^{\ell} |\mathbf{I}_N, \mathbf{J}_M, 0\rangle$ with $\ell = 0$ and $\ell = 1, \dots, N - 2M$, respectively, see Supplemental material (SM) [68]. The energy and momentum of the model are given by

$$E = \sum_i k_i^2, \quad K = \frac{2\pi}{L} \left(\sum_i I_i - \sum_{\alpha} J_{\alpha} \right), \quad (3)$$

respectively.

Initial state, density matrix and form factor. We consider the ground state of $N - 1$ spin-up delta-function

interacting bosons $|\Omega\rangle$ as a medium, and one spin-down atom with a wave function $\phi_{\downarrow}(x)$ as an injected impurity. This gives an initial state $|\Phi_{\downarrow}\rangle = \int dx \phi_{\downarrow}(x) \hat{\Psi}_{\downarrow}^{\dagger}(x) |\Omega\rangle$. Thus the time evolution of density matrix of the spin-down boson is given by

$$\rho_{\downarrow}(x, x', t) = \frac{\langle \Phi_{\downarrow} | \hat{\Psi}_{\downarrow}^{\dagger}(x, t) \hat{\Psi}_{\downarrow}(x', t) | \Phi_{\downarrow} \rangle}{\langle \Phi_{\downarrow} | \Phi_{\downarrow} \rangle}$$

$$= \sum_{\alpha, \alpha'} e^{i(E_{\alpha} - E_{\alpha'})t} A_{\alpha}^* A_{\alpha'} \rho_{\downarrow}^{\alpha\alpha'}(x, x'), \quad (4)$$

where $\hat{\Psi}_{\sigma}^{\dagger}(x, t) = e^{i\hat{H}t} \hat{\Psi}_{\sigma}^{\dagger}(x) e^{-i\hat{H}t}$, $\rho_{\downarrow}^{\alpha\alpha'}(x, x') = \langle \alpha | \hat{\Psi}_{\downarrow}^{\dagger}(x) \hat{\Psi}_{\downarrow}(x') | \alpha' \rangle / \sqrt{\langle \alpha | \alpha \rangle \langle \alpha' | \alpha' \rangle}$ is the matrix element of the density operator and A is the overlap between the initial state and the eigenstates, $A_{\alpha} = \langle \alpha | \Phi_{\downarrow} \rangle / \sqrt{\langle \alpha | \Phi_{\downarrow} \rangle}$. $|\alpha\rangle$ is the highest weight state denoted by $|\mathbf{I}_N, \mathbf{J}, 0\rangle$ or the non-highest weight state $|\mathbf{I}_N, \mathbf{J}_0, 1\rangle$, E_{α} is the energy of the state $|\alpha\rangle$, here \mathbf{J}_0 denotes an empty set. The non-highest state was largely ignored in literature, here we notice its nontrivial contributions to the impurity dynamics, see SM [68]. Using the determinant representation [35, 69–73], we precisely calculate the overlapping integral A_{α} and the density matrix $\rho_{\downarrow}^{\alpha\alpha'}(x, x')$. Without losing generality, we will take the impurity wave packet as a plane wave with momentum Q , i.e. $\phi_{\downarrow}(x) = e^{iQx}$, and the corresponding the projected states have a fixed total momentum, i.e., $K = Q$, the momentum is conserved in the states $|\alpha\rangle$. This naturally gives a selection rule of the overlap A_{α} and the matrix element. With the help of the sum rule of A_{α} , we may select enough essential states such that the sum rule is very close to 1, see SM [68] for details. Here we would like to emphasize that, to analyze the microscopic origin of physical phenomena, a subspace with proper truncation can be efficient [11–15]. The single particle-hole excitations with hole nearby the Fermi surface present the most essential ones for the long time limit behavior [12]. In contrast, here we selected the projected pairs of states, i.e. the magnon- and exciton-like states, to discuss the periodicities of QF and QR.

Microscopic origin of Quantum flutter. The time evolution of the impurity momentum is given by $K_{\downarrow}(t) = \sum_{k_n} k_n P_{\downarrow}(k_n, t)$, here the Fourier component $k_n = 2n\pi/L$, $n = 0, \pm 1, \dots$ and the probability of impurity in momentum space is given by

$$P_{\downarrow}(k_n, t) = \int \rho_{\downarrow}(x, 0, t) e^{ik_n x} dx \quad (5)$$

$$= \sum_{\alpha, \alpha'} e^{i(E_{\alpha} - E_{\alpha'})t} A_{\alpha}^* A_{\alpha'} \int \rho_{\downarrow}^{\alpha\alpha'}(x, 0) e^{ik_n x} dx.$$

Using the BA solution of Eq. (2) and its form factor, see [68], we rigorously calculate the time evolution of the distribution $P_{\downarrow}(k_n, t)$ in FIG 1 (a), showing a QF wave-like oscillation near $k_n = -0.4k_F$ and the revival at the original momentum $k_n = Q$. In FIG. 1 (b), we shows

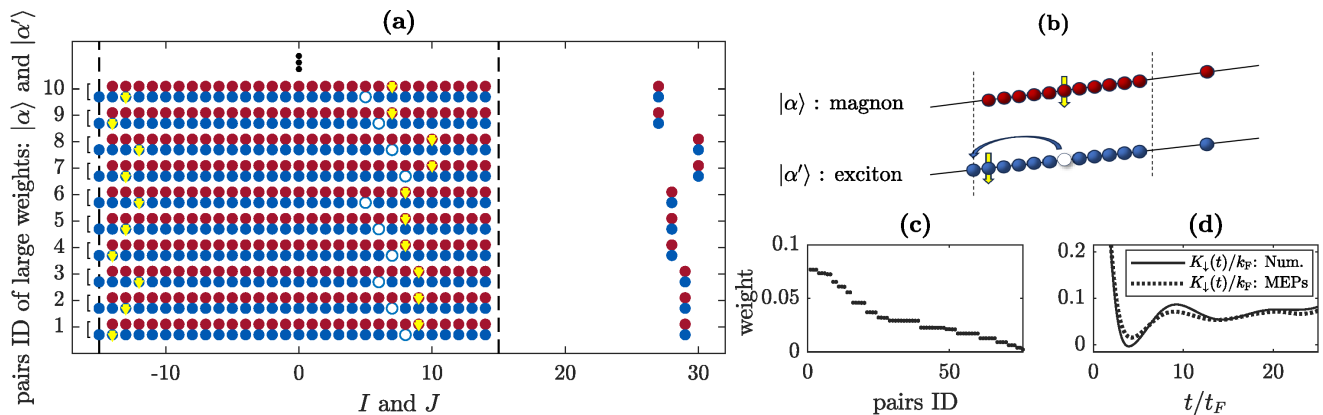


FIG. 2. Selected microscopic states of the QF with $Q = 1.33k_F$, $N = 30$, and $\gamma = 10$. (a) The macroscopic MEPs of $|\alpha\rangle$ and $|\alpha'\rangle$ have large contributions to the QF. The dots always stand for the quantum numbers I_N and the yellow-arrow \downarrow indicates the position of the quantum number J . The rows with red dots denote the magnon-like states and the ones with blue dots denote the exciton-like states. (b) Schematic illustration of the magnon- and exciton-like states. The former (red) has an emitted particle outside the Fermi sea, and a spin-down particle sits near the center. In the latter (blue), a particle in the deep Fermi sea excites onto the Fermi surface, while a down-spin sits near the left Fermi point and the emitted particle sits outside the Fermi sea. (c) We show the contributions from the MEPs pairs with high weights $|A_\alpha|^2 + |A_{\alpha'}|^2$. Here we normalized the sum rule weights by the largest one. (d) The black solid line stands for the numerical result of $K_\downarrow(t)$, whereas the black dotted line shows the result obtained from the selected MEPs.

that a coherent oscillation of the impurity momentum $K_\downarrow(t)$ occurs soon after a quick decay, also see later discussion in FIG. 2 (d) and FIG. 3 (c). The QF dynamics drastically comes from the coherent transition between the magnon excitations and particle-hole collective excitations resulted in from the impurity scattering with the atoms in the interacting medium, which we simply call magnon- and exciton-like states, respectively.

From Eq. (5), we observe that the time evolution of the momentum distribution $P_\downarrow(k_n, t)$ depends on the energy differences $E_\alpha - E_{\alpha'}$ between the particle-hole excitations and exciton-like excitations, which determine the oscillation periodicity $\tau_{\text{QF}} \sim 2\pi/|E_\alpha - E_{\alpha'}|$. This naturally suggests a mechanism for the supersonic behaviour, i.e. coherent transition between the states $\{|\alpha\rangle, |\alpha'\rangle\}$. Being guided by the sum rule weights, in FIG. 2 (a), for $N = 30$, we find that the 10 pairs of states $\{|\alpha\rangle, |\alpha'\rangle\}$ with the high sum rule weights mainly capture the dynamics of $P_\downarrow(k_n, t)$ and $K_\downarrow(t)$. Here we used the same setting as that for the FIG. 1. While FIG. 2 (b) presents a schematic illustration of the magnon- and exciton-like states of these pairs (states $|\alpha\rangle$ and $|\alpha'\rangle$). In FIG. 2 (c), we give the high weights of these excitation pairs $|A_\alpha|^2 + |A_{\alpha'}|^2$, showing the contribution of each magnon-exciton pair (MEP) to the dynamical evolution of the impurity. In FIG. 2 (d), we show that the $K_\downarrow(t)$ obtained from the selected MEPs (black dotted line) coincides with the numerical result (black solid line) from the BA wave function. This remarkably indicates that the microscopic MEPs result in the coherent transitions between $|\alpha\rangle$ and $|\alpha'\rangle$ states with the almost same energy difference [68].

We further obtain the periodicity of the QF

$$\tau_{\text{QF}} = \frac{2\pi}{|\varepsilon_c(0)| - |\varepsilon_s(0)|}. \quad (6)$$

Where the charge and spin dressed energies are determined by $\varepsilon_c(k) = k^2 - \mu - \int_{-k_0}^{k_0} a_2(k - k')\varepsilon_c(k')dk'$, $\varepsilon_s(\lambda) = - \int_{-k_0}^{k_0} a_1(k - \lambda)\varepsilon_c(k)dk$, respectively [68]. Here we denoted $a_n(x) = \frac{1}{2\pi} \frac{nc}{(nc/2)^2 + x^2}$, μ is the chemical potential, k_0 is the Fermi point (cut-off) of charge quasi-momentum k , $\varepsilon_c(k_0) = 0$ and $\varepsilon_s(\pm\infty) = 0$. FIG 3 (a) shows the oscillation period v.s. the interaction strength, confirming an agreement between the analytical result (blue solid line) Eq. (6) and the numerical result (circles). The period of the QF decreases with an increase of the interaction γ . For a strong coupling, we have $\tau_{\text{QF}} = 2\pi t_F(1 + 20/3\gamma)$ (long dashed line), where the $t_F = 1/E_F$ with the Fermi energy $E_F = k_F^2$. In the Tonks limit, i.e. $\gamma \rightarrow \infty$, $\Delta E_{\text{QF}} = E_F$ and thus $\tau_{\text{QF}} = 2\pi t_F$ (blue dotted line).

Moreover, we note that the period of the QF dose not depend on the injected momentum Q . We calculate the QF dynamics for several values of the injected momenta and find that the QF always appears for $Q > k_F$ and oscillating amplitude rises slightly as the increase of Q , see FIG 3 (c). In addition, using the Gaussian impurity wave packet [68], we further observe that the motion of mass center of the impurity $X_\downarrow(t) = \langle \Phi_I | \hat{x}(t) | \Phi_I \rangle / \langle \Phi_I | \Phi_I \rangle$ coincide with the evolution of the impurity momentum, namely, $\frac{1}{2} \partial_t X_\downarrow(t) = K_\downarrow(t)$, see [68].

Quantum revival and Bloch oscillation FIG. 1 (a) showed another periodic revival behavior appearing along

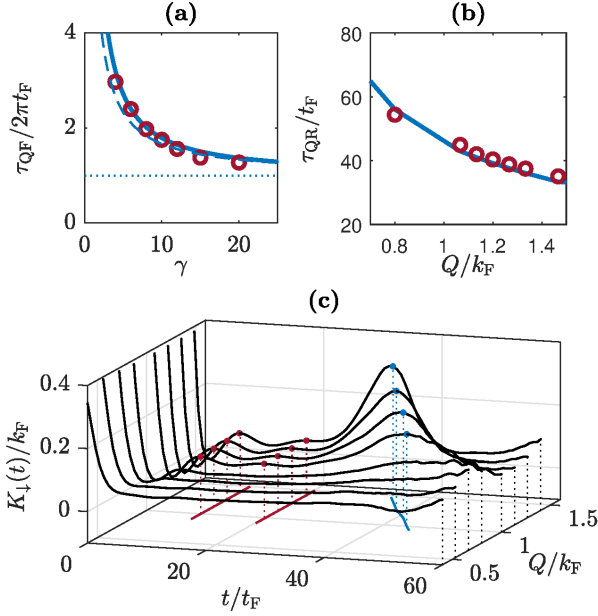


FIG. 3. (a) The blue solid line shows the period of the QF calculated by using Eq. (6), showing a good agreement with the numerical result (circles) obtained from the states of MPs pairs. The blue dotted (long dashed) line denotes the result of $\tau_{\text{QF}} = 2\pi t_{\text{F}}$ in the Tonks limit (strong coupling region $\tau_{\text{QF}} = 2\pi t_{\text{F}}(1 + 20/3\gamma)$). (b) The larger periodic revival of $K_{\downarrow}(t)$ (blue solid) obtained from Eq. (7) agrees well with the numerical result (circles) obtained from the states of MPs pairs. (c) shows the dynamics of the QF and QR of the impurity with different values of initial momentum Q for fixed interaction strength $\gamma = 10$ and particle number $N = 30$. The red and blue solid lines show the periodicities of the QF and QR, respectively.

the line $k_n = Q$, also see the evolution of momentum $K_{\downarrow}(t)$ in FIG. 3 (c). This striking feature is essentially related to the quantum reflection of excitations induced by the periodic boundary conditions. Using BA equations (2), we determine a set of pairs of magnon-like states with the same minimum momentum difference that have large sum rule weights for the QR dynamics of the impurity, see [68]. Here we precisely determine that pairs of magnon states have a minimum momentum difference $\Delta p = 2\pi/L$ lead to an energy difference $\Delta E_L = [v_c(Q - k^*) - v_s(k^*)]\Delta p$, where the sound velocities of the charge and magnon excitations are given by $v_{c,s}(p) = \partial E_{c,s}(p)/\partial p$, and $E_{c,s}(p)$ the single particle dispersions of charge and spin, respectively. Consequently, the period of QR is given by

$$\tau_{\text{QR}} = \frac{L}{v_c(Q - k^*) - v_s(k^*)}, \quad (7)$$

when $Q > k_{\text{F}}$, the k^* can be numerically determined by the magnon-like state with the largest weight $|A_{\alpha}|^2$,

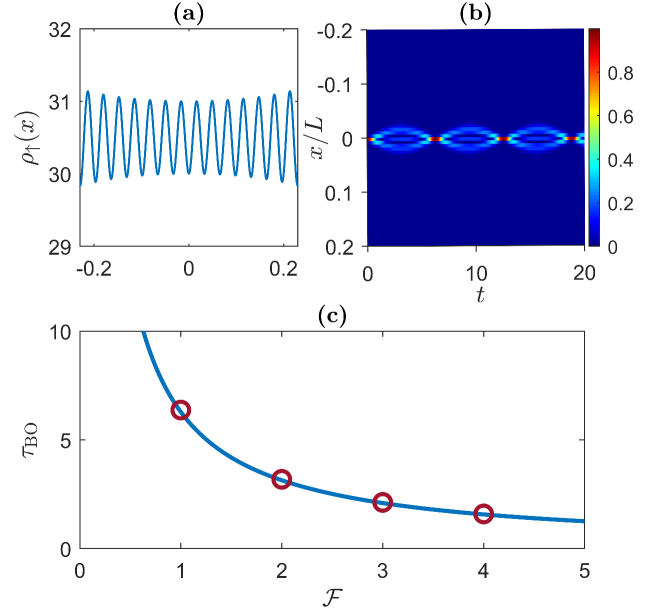


FIG. 4. The Bloch oscillations of the magnon impurity. We set $N = L = 30$, and $c_{\text{IB}} = 1$ for our numerical calculation. (a) shows the density profile $\rho_{\uparrow}(x)$ of the medium in the ground state of the Lieb-Liniger Hamiltonian H_{LL} with an infinite interaction strength. (b) shows the time evolution of density distribution of the impurity under the Hamiltonian (8) with $\mathcal{F} = 1$. (c) The solid line shows the period of BO $\tau_{\text{BO}} = 2\pi/\mathcal{F}$ with respect to the gradient field \mathcal{F} , the circles denote the numerical results.

namely, we have $k^* = (1 - 2J/N)k_{\text{F}}$, here $0 < k^* < k_{\text{F}}$. The value k^* is related to the quantum number of the BA state with the highest projection weight. A deep insight into the QR can be conceived from the impurity momentum $\tilde{K}_{\downarrow}(E)$ in frequency space, see SM [68]. The QR is also observed in the single particle propagator [68].

On the other hand, the model (1) also provides a promising metrological resource for measuring gravitational force via the following experimentally realizable Hamiltonian [11] $H_{\text{BO}} = H_{\text{LL}} + T_{\text{Im}} + \int_0^L dx (c_{\text{IB}} \sum_{\sigma=\uparrow} \hat{\Psi}_{\sigma}^{\dagger} \hat{\Psi}_{\sigma} \hat{\Psi}_{\downarrow}^{\dagger} \hat{\Psi}_{\downarrow} + \mathcal{F}x \hat{\Psi}_{\downarrow}^{\dagger} \hat{\Psi}_{\downarrow}) dx$, where $H_{\text{LL}} = \int_0^L dx (\partial \hat{\Psi}_{\uparrow}^{\dagger} \partial \hat{\Psi}_{\uparrow} + c \hat{\Psi}_{\uparrow}^{\dagger} \hat{\Psi}_{\uparrow} \hat{\Psi}_{\uparrow}^{\dagger} \hat{\Psi}_{\uparrow})$ is the spinless Lieb-Liniger gas of model (1), T_{Im} is the kinetic energy of the impurity, c_{IB} denotes the interaction between the impurity and the medium, and \mathcal{F} is the gravitational potential. Here we consider the TG gas as the interacting medium H_{LL} such that the density distribution $\rho_{\uparrow}(x) = \langle \hat{\Psi}_{\uparrow}^{\dagger}(x) \hat{\Psi}_{\uparrow}(x) \rangle$ in the medium naturally provides a periodic potential as a 1D lattice. Using the result of the wave function given in [80], we demonstrate such an existence of an ideal 1D lattice structure of the density profile in the central region of the medium, see FIG. 4 (a). Based on this observation, we can further regard

the effective Hamiltonian H_{BO} as

$$H_{\text{BO}} \approx T_{\text{Im}} + \int_0^L \left(c_{\text{IB}} \hat{\rho}_{\downarrow}(x) \rho_{\uparrow}(x) + \mathcal{F} x \hat{\rho}_{\downarrow}(x) \right) dx. \quad (8)$$

In FIG. 4 (b), we set the initial state with the impurity at the center of the center of the medium ($x = 0$). The impurity is accelerated by gravitational force \mathcal{F} , and the impurity interaction with the medium $c_{\text{IB}} \rho_{\uparrow}(x)$ provides a periodic potential, keeping the momentum of the impurity in the Brillouin zone. Consequently, we observe the Bloch oscillation (BO) with the periodicity given by $\tau_{\text{BO}} = 2\pi/\mathcal{F}$, see Fig. 4 (c). This provides a useable metrological application of the magnon impurity for measuring the gravitational constant g through the BO. From a perspective of the quantum resource theory, applications of magnon impurities in sensing gravitational force and external magnetic field are plausible [74, 81, 82].

In summary, using BA and form factor, we have rigorously determined microscopic states for QF and QR of a supersonic impurity injected into the 1D medium of interacting bosons. We have obtained explicit expressions of the periods of the QF (6) and the QR (7), revealing deep insights into the coherent features of the magnon- and exciton-like states in the course of impurity scattering with the interacting medium. Based on the current experimental capability of realizing the 1D impurity problems [11, 66, 67], measurement of the supersonic behaviour of the model (1) can be readily implemented through highly elongated 1D systems of selective ultracold atoms. Finally, we have proposed a metrological application of the quantum impurity in sensing the gravitational force. Our results provide an extended understanding of the quantum supersonic impurities in the 1D interacting medium of Luttinger liquids.

ACKNOWLEDGEMENT

X.W.G and Y.Z.J. are supported by the NSFC key grants No. 12134015, No. 92365202, No. 12121004, No. 12175290 and the National Key R&D Program of China under grants No. 2022YFA1404102. They also partially supported by the Innovation Program for Quantum Science and Technology 2021ZD0302000, the Peng Huanwu Center for Fundamental Theory, No. 12247103, and the Natural Science Foundation of Hubei Province 2021CFA027. H.Q.L acknowledges financial support from NSFC12088101.

* jiangyuzhu@wipm.ac.cn

† hqlin@zju.edu.cn

‡ xiwen.guan@anu.edu.au

[1] A. Schirotzek, C.-H. Wu, A. Sommer, and M. W. Zwierlein, Phys. Rev. Lett. **102**, 230402 (2009).

- [2] S. Nascimbène, N. Navon, K. J. Jiang, L. Tarruell, M. Teichmann, J. McKeever, F. Chevy and C. Salomon, Phys. Rev. Lett. **103**, 170402 (2009).
- [3] R. Combescot and S. Giraud, Phys. Rev. Lett. **101**, 050404 (2008).
- [4] G. M. Bruun and P. Massignan, Phys. Rev. Lett. **101**, 050404 (2010).
- [5] Z. Z. Yan, Y. Ni, C. Robens, and M. W. Zwierlein, Science **368**, 190 (2020).
- [6] S. I. Mistakidis, G. C. Katsimiga, G. M. Koutentakis, T. Busch, and P. Schmelcher, Phys. Rev. Lett. **122**, 183001 (2019).
- [7] B. M. Henson, X. G. Yue, S. S. Hodgman, D. K. Shin, L. A. Smirnov, E. A. Ostrovskaya, X. W. Guan, A. G. Truscott, Phys. Rev. A **97**, 063601 (2018).
- [8] B. Doyon, J. Dubail, R. Konik, and T. Yoshimura, Phys. Rev. Lett. **119**, 195301 (2017).
- [9] S. A. Simmons, F. A. Bayococ, J. C. Pillay, D. Colas, I. P. McCulloch, and K. V. Kheruntsyan, Phys. Rev. Lett. **125**, 180401 (2020).
- [10] J. Li, S. Chockalingam, and T. Cohen, Phys. Rev. Lett. **127**, 014302 (2021).
- [11] F. Meinert, et. al. Science **356**, 945 (2017)
- [12] C. J. M. Mathy, M. B. Zvonarev, and E. Demler, Nat. Phys. **8**, 881 (2012).
- [13] M. Knap, C. J. M. Mathy, M. Ganahl, M. B. Zvonarev, and E. Demler, Phys. Rev. Lett. **112**, 015302 (2014).
- [14] R. van den Berg, B. Wouters, S. Eliëns, J. De Nardis, R. M. Konik, and J.-S. Caux, Phys. Rev. Lett. **116**, 225302 (2016).
- [15] W. S. Bakr, J. I. Gillen, A. Peng, S. Foelling, and M. Greiner, Nature **462**, 74 (2009).
- [16] P. M. Preiss, R. Ma, M. E. Tai, A. Lukin, M. Rispoli, P. Zupancic, Y. Lahini, R. Islam, and M. Greiner, Science **347**, 1229 (2015).
- [17] C. Gross and I. Bloch, Science **357**, 995 (2017).
- [18] C. C. Chien, S. Peotta, and M. Di Ventra, Nat. Phys. **11**, 998 (2015).
- [19] C. Weitenberg, M. Endres, J. F. Sherson, M. Cheneau, P. Schauß, T. Fukuhara, I. Bloch, S. Kuhr, nature **471**, 319 (2011).
- [20] Y. Ashida, T. Shi, M. C. Bañuls, J. I. Cirac, and E. Demler, Phys. Rev. Lett. **121**, 026805 (2018).
- [21] J. P. Ronzheimer, M. Schreiber, S. Braun, S. S. Hodgman, S. Langer, I. P. McCulloch, F. Heidrich-Meisner, I. Bloch, and U. Schneider, Phys. Rev. Lett. **110** (2013).
- [22] T. Fukuhara, A. Kantian, M. Endres, M. Cheneau, P. Schauss, S. Hild, D. Bellem, U. Schollwoeck, T. Giamarchi, C. Gross, et al., Nat. Phys. **9**, 235 (2013).
- [23] T. Fukuhara, P. Schauss, M. Endres, S. Hild, M. Cheneau, I. Bloch, and C. Gross, nature **502**, 76 (2013).
- [24] F. Schmidt, D. Mayer, Q. Bouton, D. Adam, T. Lausch, N. Spethmann, and A. Widera, Phys. Rev. Lett. **121**, 130403 (2018).
- [25] M. Yang, M. Cufar, E. Pahl, and J. Brand, Condens. Matter **7**, 15 (2022).
- [26] R. S. Christensen, J. Levinsen, and G. M. Bruun, Phys. Rev. Lett. **115** (2015).
- [27] A. Vashisht, M. Richard, and A. Minguzzi, SciPost Phys. **12**, 008 (2022).
- [28] R. Mao, X. W. Guan, and B. Wu, Phys. Rev. A **94**, 043645 (2016).
- [29] F. Massel, A. Kantian, A. J. Daley, T. Giamarchi, and P. Torma, New J. Phys. **15**, 045018 (2013).

- [30] S. Peotta, D. Rossini, M. Polini, F. Minardi, and R. Fazio, *Phys. Rev. Lett.* **110**, 015302 (2013).
- [31] N. J. Robinson, J.-S. Caux, and R. M. Konik, *J. Stat. Mech.* **2020**, 013103 (2020).
- [32] N. J. Robinson, J.-S. Caux, and R. M. Konik, *Phys. Rev. Lett.* **116**, 145302 (2016).
- [33] H. Fröml, A. Chiocchetta, C. Kollath, and S. Diehl, *Phys. Rev. Lett.* **122**, 040402 (2019).
- [34] M. B. Zvonarev, V. V. Cheianov, and T. Giamarchi, *Phys. Rev. Lett.* **99**, 240404 (2007).
- [35] B. Pozsgay, W.-V. v. G. Oei, and M. Kormos, *J. Phys. A: Math. Theor* **45**, 465007 (2012).
- [36] N. J. Robinson and R. M. Konik, *J. Stat. Mech.*, 063101 (2017).
- [37] M. A. Cazalilla, R. Citro, T. Giamarchi, E. Orignac and M. Rigol, *Rev. Mod. Phys.* **83** 1405 (2011).
- [38] X. W. Guan, M. T. Batchelor and C. Lee, *Rev. Mod. Phys.* **85**, 1633 (2013).
- [39] X. W. Guan, P. He, *Rep. Prog. Phys.* **85** 11400 (2022).
- [40] Y. Jiang, Y.-Y. Chen, and X.-W. Guan, *Chinese Phys. B* **24**, 050311 (2015).
- [41] P. E. Dolgirev, Y.-F. Qu, M. B. Zvonarev, T. Shi, and E. Demler, *Phys. Rev. X* **11**, 041015 (2021).
- [42] N. Andrei, K. Furuya, and J. H. Lowenstein, *Rev. Mod. Phys.* **55**, 331 (1983).
- [43] E. H. Lieb and W. Liniger, *Phys. Rev.* **130**, 1605 (1963).
- [44] C. N. Yang, *Phys. Rev. Lett.* **19**, 1312 (1967).
- [45] M. Gaudin, *Phys. Lett. A* **24**, 55 (1967).
- [46] J. Vijayan, et. al. *Nature* 565, **56** (2020).
- [47] R. Senaratne, et. al. *Science* **376**, 1305 (2022).
- [48] J. B. McGuire, *J. Math. Phys.* **6**, 432 (1965); *J. Math. Phys.* **7**, 123 (1966).
- [49] X.-W. Guan, *Front. Phys.* **7**, 8 (2012).
- [50] T. L. Schmidt, G. Dolcetto, C. J. Pedder, K. Le Hur, and P. P. Orth, *Phys. Rev. Lett.* **123**, 075302 (2019).
- [51] A. S. Dehkharghani, A. G. Volosniev, and N. T. Zinner, *Phys. Rev. Lett.* **121**, 080405 (2018).
- [52] S. I. Mistakidis, F. Grusdt, G. M. Koutentakis, and P. Schmelcher, *New J. Phys.* **21**, 103026 (2019).
- [53] J.-S. Caux, A. Klauser, and J. van den Brink, *Phys. Rev. A* **80** (2009).
- [54] J. N. Fuchs, D. M. Gangardt, T. Keilmann, and G. V. Shlyapnikov, *Phys. Rev. Lett.* **95**, 150402 (2005).
- [55] M. T. Batchelor, M. Bortz, X.-W. Guan and N. Oelkers, *J. Stat. Mech.*, P03016 (2006).
- [56] L. Amico, et. al. *AVS Quantum Sci.* **3**, 039201 (2021).
- [57] F. Scazza, J. Levinsen, M. Zaccanti, P. Massignan, M. M. Parish, *Atoms* **2022**, 10, 55.
- [58] E. Eisenberg, and E. H. Lieb, *Phys. Rev. Lett.* **89**, 220403 (2002)
- [59] X.-W. Guan, M. T. Batchelor and M. Takahashi, *Phys. Rev. A* **76**, 043617 (2007).
- [60] R. E. Barfknecht, A. Foerster, and N. T. Zinner, *Few-Body Syst* **59**:22 (2018).
- [61] O. I. Patu, A. Klümper, and A. Foerster, *Phys. Rev. Lett.* **120**, 243402 (2018).
- [62] M. Olshanii, *Phys. Rev. Lett.* **81**, 938 (1998).
- [63] Y.-Q. Li, S.-J. Gu, Z.-J. Ying, U. Eckern, *EuroPhys. Lett.* **61**, 368 (2003).
- [64] C. N. Yang, *Phys. Rev. Lett.* **19**, 1312 (1967).
- [65] B. Sutherland, *Phys. Rev. Lett.* **20**, 98 (1968).
- [66] S. Palzer, C. Zipkes, C. Sias and M. Köhl, *Phys. Rev. Lett.* **103**, 150601 (2009).
- [67] J. Catani, G. Lamporesi, D. Nailk, M. Gring, M. Inguscio, F. Minardi, A. Kantian and T. Giamarchi, *Phys. Rev. A* **85**, 023623 (2012).
- [68] In this supplemental material, we introduce the form factor formula of Bethe ansatz states and present in detail the calculation of the time evolution of the impurity dynamics as well as analytical analysis on the oscillation features of quantum flutter and revival.
- [69] J.-S. Caux, and P. Calabrese, *Phys. Rev. A* **74**, 031605(R) (2006)
- [70] J.-S. Caux, P. Calabrese, and N. A. Slavnov, *J. Stat. Mech.*, P01008 (2007).
- [71] J.-S. Caux, *J. Math. Phys.* **50**, 095214 (2009).
- [72] S. Cheng, Y.-Y. Chen, X.-W. Guan, W.-L. Yang, R. Mondaini, and H.-Q. Lin, arXiv:2209.15221v1.
- [73] R.-T. Li, S. Cheng, Y.-Y. Chen, X.-W. Guan, arXiv:2303.09208.
- [74] Q.-K. Wan, H.-L. Shi and X.-W. Guan, *Phs. Rev. B* **109**, L041301 (2024).
- [75] E. Burovski, V. Cheianov, O. Gamayun, and O. Lychkovskiy, *Phys. Rev. A* **89**, 041601(R) (2014).
- [76] O. Gamayun, O. Lychkovskiy, E. Burovski, M. Malcolmson, V. V. Cheianov, and M. B. Zvonarev, *Phys. Rev. Lett.* **120**, 220605 (2018).
- [77] O. Gamayun, O. Lychkovskiy, and M. B. Zvonarev, *SciPost. Phys.* **8**, 053 (2020).
- [78] O. Gamayun, O. Lychkovskiy, and J.-S. Caux, *SciPost. Phys.* **8**, 036 (2020).
- [79] O. Gamayun, M. Panfil, F. T. Sant'Ana, *Phys. Rev. Res.* **5**, 043265 (2023).
- [80] E. Nandani, R. A. Romer, S. Tan, and X. W. Guan, *New J. Rhsy.* **18**, 55014 (2016).
- [81] L. Yang, and H. Pu, *Phys. Rev. A* **95**, 051602(R) (2017).
- [82] X. Cai, H. Yang, H.-L. Shi, C. Lee, N. Andrei and X. W. Guan, *Phys. Rev. Lett.* **127**(10), 100406 (2021).

Microscopic origin of quantum supersonic phenomenon in one dimension

— Supplementary materials

Zhe-Hao Zhang, Yuzhu Jiang, Hai-Qing Lin, and Xi-Wen Guan

S1. THE ONE-DIMENSIONAL TWO-COMPONENT BOSE GAS

The model Eq. (1) in the main text describes the one-dimensional (1D) two-component Bose gases with a delta-function interaction. As a solvable many-body problem, its Hamiltonian reads

$$\hat{H} = - \sum_{i=1}^N \frac{\partial^2}{\partial x_i^2} + 2c \sum_{i < j} \delta(x_i - x_j), \quad (\text{s1})$$

where N is the total particle number, c is the interaction strength and L is length of the system. Here we take the periodic boundary conditions and the total momentum \hat{K} is conserved. The eigenstate of N particles with M spin-down bosons of the model Eq. (1) in the main text is given by

$$|\Psi\rangle = \int d\mathbf{x} \Psi(\mathbf{x}) \hat{\Psi}_{\downarrow}^{\dagger}(x_1) \hat{\Psi}_{\downarrow}^{\dagger}(x_2) \cdots \hat{\Psi}_{\downarrow}^{\dagger}(x_M) \times \hat{\Psi}_{\uparrow}^{\dagger}(x_{M+1}) \hat{\Psi}_{\uparrow}^{\dagger}(x_{M+2}) \cdots \hat{\Psi}_{\uparrow}^{\dagger}(x_N) |0\rangle, \quad (\text{s2})$$

where $\hat{\Psi}_{\uparrow, \downarrow}^{\dagger}(x)$ are the field operators of spin-up and spin-down bosons, respectively, $\Psi(\mathbf{x})$ denotes the Bethe ansatz (BA) wave function of the first quantized Hamiltonian (s1). Here we denoted $\mathbf{x} = \{x_1, x_2, \dots, x_N\}$, $\int d\mathbf{x} = \int_0^L dx_1 \int_0^L dx_2 \cdots \int_0^L dx_N$ and $|0\rangle$ stands for the vacuum state.

This model was exactly solved by the BA [1–3] and the Bethe ansatz equations (BAE) are given by

$$e^{ik_j L} = - \prod_{j'=1}^N \frac{k_j - k_{j'} + ic}{k_j - k_{j'} - ic} \prod_{\alpha=1}^M \frac{k_j - \lambda_{\alpha} - ic/2}{k_j - \lambda_{\alpha} + ic/2}, \quad (\text{s3})$$

$$\prod_{j=1}^N \frac{\lambda_{\alpha} - k_j - ic/2}{\lambda_{\alpha} - k_j + ic/2} = - \prod_{\beta=1}^M \frac{\lambda_{\alpha} - \lambda_{\beta} - ic}{\lambda_{\alpha} - \lambda_{\beta} + ic},$$

where k_j is the wave number, λ_{α} is the spin rapidity, $j = 1, 2, \dots, N$ and $\alpha = 1, 2, \dots, M$. Eqs. (2) in the main text were obtained from the logarithm form of the BAE (s3). Both the energy and momentum are conserved and they are given by

$$E = \sum_{j=1}^N k_j^2, \quad K = \sum_{j=1}^N k_j, \quad (\text{s4})$$

respectively. Moreover, the total momentum can be calculated by the quantum numbers of the logarithm form of BAE, see Eq. (3) in the main text.

S2. QUANTUM DYNAMICS OF THE SUPERSONIC IMPURITY

We first discuss the evolution of impurity momentum injected into a bosonic quantum medium. The medium is the ground state of $N - 1$ spin-up bosons $|\Omega\rangle$, and the impurity is a spin-down particle with a wave function $\phi_{\downarrow}(x)$. We define the initial state of the supersonic impurity

$$|\Phi_{\text{I}}\rangle = \int_0^L dx \phi_{\downarrow}(x) \hat{\Psi}_{\downarrow}^{\dagger}(x) |\Omega\rangle. \quad (\text{s5})$$

The time evolution of the impurity momentum is defined by

$$K_{\downarrow}(t) = \sum_{k_n} k_n P_{\downarrow}(k_n, t), \quad (\text{s6})$$

where $P_{\downarrow}(k_n, t)$ is the momentum distribution

$$P_{\downarrow}(k_n, t) = \frac{1}{L} \int_0^L dx \int_0^L dx' e^{-ik_n(x-x')} \times \frac{\langle \Phi_{\text{I}} | \hat{\Psi}_{\downarrow}^{\dagger}(x, t) \hat{\Psi}_{\downarrow}(x', t) | \Phi_{\text{I}} \rangle}{\langle \Phi_{\text{I}} | \Phi_{\text{I}} \rangle}, \quad (\text{s7})$$

$\hat{\Psi}_{\downarrow}^{\dagger}(x, t) = e^{i(\hat{H}t - \hat{K}x)} \hat{\Psi}_{\downarrow}^{\dagger}(0) e^{-i(\hat{H}t - \hat{K}x)}$ and $k_n = 2n\pi/L$, $n = 0, \pm 1, \dots$. Insert three complete sets of eigenstates into $P_{\downarrow}(k_n, t)$, we get

$$P_{\downarrow}(k_n, t) = k_n L \sum_{\alpha\alpha'} e^{i(E_{\alpha} - E_{\alpha'})t} \delta_{k_n, K_{\alpha} - K_{\beta}} \delta_{K_{\alpha}, K_{\alpha'}} \times \frac{\langle \Phi_{\text{I}} | \alpha \rangle \langle \alpha | \hat{\Psi}_{\downarrow}^{\dagger}(0) | \beta \rangle \langle \beta | \hat{\Psi}_{\downarrow}(0) | \alpha' \rangle \langle \alpha' | \Phi_{\text{I}} \rangle}{\langle \Phi_{\text{I}} | \alpha \rangle \langle \beta | \alpha' \rangle}, \quad (\text{s8})$$

where $|\alpha\rangle$, $|\alpha'\rangle$ and $|\beta\rangle$ are eigenstates of the Hamiltonian and momentum, namely, $H|\alpha\rangle = E_{\alpha}|\alpha\rangle$ and $\hat{K}|\alpha\rangle = K_{\alpha}|\alpha\rangle$. Thus the time evolution of impurity momentum can be written as

$$K_{\downarrow}(t) = L \sum_{\alpha\alpha'} e^{i(E_{\alpha} - E_{\alpha'})t} K_{\alpha\alpha'}, \quad (\text{s9})$$

$$K_{\alpha\alpha'} = \sum_{\beta} (K_{\alpha} - K_{\beta}) A_{\alpha}^* B_{\alpha\beta}^* B_{\alpha'\beta} A_{\alpha'} \delta_{K_{\alpha}, K_{\alpha'}},$$

where A is the overlap between the initial state and the eigenstate, $A_{\alpha} = \langle \alpha | \Phi_{\text{I}} \rangle / \sqrt{\langle \alpha | \alpha \rangle \langle \Phi_{\text{I}} | \Phi_{\text{I}} \rangle}$ and matrix element $B_{\alpha\beta} = \langle \beta | \hat{\Psi}_{\downarrow}(0) | \alpha \rangle / \sqrt{\langle \alpha | \alpha \rangle \langle \beta | \beta \rangle}$. The sum rule of A_{α} and $B_{\alpha\beta}$ are

$$\sum_{\alpha} |A_{\alpha}|^2 = 1, \quad L \sum_{\beta} |B_{\alpha\beta}|^2 = 1, \quad (\text{s10})$$

respectively, and $|A_\alpha|^2$ ($|B_{\alpha\beta}|^2$) is the weight of eigenstate $|\alpha\rangle$ in the overlap (density matrix element).

Using the eigenstates of Hamiltonian (s1), we can calculate the eigenvalues of the Hamiltonian, the overlap A_α and the matrix elements $B_{\alpha\beta}$ in terms of determinant representation of the norms and form factors. Consequently, we may obtain the evolutions of the momentum and momentum distributions. In particular, guided by the sum rules, we can select the microscopic states with large sum rule weights that essentially comprise the oscillation features of the QF and revival dynamics. We give in details the calculations of the above mentioned quantities in next sections.

S3. METHOD FOR CALCULATING TIME EVOLUTION OF IMPURITY MOMENTUM

S3.1 Selection of the eigenstates for quantum flutter

In the BA equations Eqs. (2) in the main text, \mathbf{I} and \mathbf{J} denote the quantum numbers of the charge and spin degrees of freedom, respectively, where $\mathbf{I} = \mathbf{I}_N = \{I_1, I_2, \dots, I_N\}$, $\mathbf{J} = \mathbf{J}_M = \{J_1, J_2, \dots, J_M\}$ and M is the number of spin-down particles. For a given set of quantum numbers $\{\mathbf{I}_N, \mathbf{J}_M\}$, the BA equations uniquely determine the wave numbers and spin rapidities $\{k_1, k_2, \dots, k_N; \lambda_1, \lambda_2, \dots, \lambda_M\}$. Consequently, one BA solution/BA highest weight state gives $N - 2M + 1$ eigenstates, $|\mathbf{I}_N, \mathbf{J}_M, \ell\rangle = (\hat{S}^-)^\ell |\mathbf{I}_N, \mathbf{J}_M, 0\rangle$, where $\ell = 0, 1, 2, \dots, N - 2M$. Here we denote $|\mathbf{I}_N, \mathbf{J}_M, 0\rangle$ as the highest weight state, i.e., $\hat{S}^+ |\mathbf{I}_N, \mathbf{J}_M, 0\rangle = 0$. The states with non-zero values of the ℓ are non-highest weight states. In the above, we defined the spin operators $\hat{S}^- = \int dx \hat{\Psi}_\downarrow^\dagger(x) \hat{\Psi}_\uparrow(x)$ and $\hat{S}^+ = \int dx \hat{\Psi}_\uparrow^\dagger(x) \hat{\Psi}_\downarrow(x)$. The total spin S and its projection in z -direction S^z are good quantum numbers of the state $|\mathbf{I}_N, \mathbf{J}_M, \ell\rangle$, namely,

$$S = N/2 - M, \quad S^z = N/2 - M - \ell. \quad (\text{s11})$$

There are three sets of complete eigenstates $\{|\alpha\rangle\}$, $\{|\alpha'\rangle\}$ and $\{|\beta\rangle\}$ which were inserted in the calculation of impurity momentum $K_\downarrow(t)$ Eq. (s9). The eigenstates include all of the highest and non-highest weight ones. Guided by the sum rules, we need to select enough states to calculate the dynamical evolutions of the momentum $K_\downarrow(t)$ and momentum distributions. Without losing accuracy, the following selection rules were used to essentially simplify our numerical task:

- (i) The total particle number is a good quantum number of the initial state $|\Phi_1\rangle$, such that $\{|\alpha\rangle\}$ and $\{|\alpha'\rangle\}$ consist of the states $|\mathbf{I}_N, \mathbf{J}_M, \ell\rangle$ with total particle number N . However, the state $\{|\beta\rangle\}$ in Eq. (s9) must be the state $|\mathbf{I}_{N-1}, \mathbf{J}_{M'}, \ell\rangle$ with the total particle number $N - 1$, respectively.

- (ii) The total spin is not a good quantum number of the initial state $|\Phi_1\rangle$, while S^z is a good quantum number, $\hat{S}^z |\Phi_1\rangle = (N/2 - 1) |\Phi_1\rangle$. Together with the selection rule (i), the possible states of $\{|\alpha\rangle\}$ and $\{|\alpha'\rangle\}$ are $|\mathbf{I}_N, \mathbf{J} = \mathbf{J}_1, 0\rangle$ and $|\mathbf{I}_N, \mathbf{J}_0, 1\rangle$. Whereas the state $\{|\beta\rangle\}$ relates to the state $|\mathbf{I}_{N-1}, \mathbf{J}_0, 0\rangle$, where \mathbf{J}_0 is an empty set.

- (iii) When the impurity wave function $\phi_\downarrow(x)$ is a plane wave with a fixed momentum Q , the total momentum is also a good quantum number of $|\Phi_1\rangle$, $\hat{K} |\Phi_1\rangle = Q |\Phi_1\rangle$, so that $\langle \mathbf{I}, \mathbf{J}_0, 1 | \Phi_1 \rangle = \langle \mathbf{I}, \mathbf{J}, 0 | \Phi_1 \rangle = 0$ when the quantum numbers do not satisfy $K = Q$ according to Eq. (3) in the main text. We only need to calculate the states with $K_\alpha = K_{\alpha'} = Q$ in our study.

Based on these selection rules, we need to obtain the states $|\mathbf{I}_N, \mathbf{J}, 0\rangle$, $|\mathbf{I}_N, \mathbf{J}_0, 1\rangle$ and $|\mathbf{I}_{N-1}, \mathbf{J}_0, 0\rangle$ (\mathbf{J}_0 is defined in selection rule (ii)). We will give these states in the following study.

For the states with all N particles spin-up, we give a set of quantum numbers \mathbf{I}_N , get a set of wave numbers $\{k_j\}$ from the BA equations (2) and find the wave function of this eigenstate to be

$$\begin{aligned} |\mathbf{I}, \mathbf{J}_0, 0\rangle &= \int d\mathbf{x} \Phi_0(\mathbf{x}) \hat{\Psi}_\uparrow^\dagger(x_1) \dots \hat{\Psi}_\uparrow^\dagger(x_N) |0\rangle, \\ \Phi_0(\mathbf{x}) &= \frac{1}{\sqrt{N!}} \sum_{\mathcal{P}} (-1)^{\mathcal{P}} e^{i \sum_j x_j k_{\mathcal{P}_j}} \\ &\quad \times \prod_{i < j} [k_{\mathcal{P}_i} - k_{\mathcal{P}_j} + ic \text{sign}(x_j - x_i)], \quad (\text{s12}) \end{aligned}$$

where \mathcal{P} are the permutations of $\{1, 2, \dots, N\}$. The total spin of this state is $S = S^z = N/2$. In fact, $|\mathbf{I}, \mathbf{J}_0, 0\rangle$ is the eigenstate of the Lieb-Liniger model.

There are two kinds of eigenstates with one spin-down particle, the highest weight states $|\mathbf{I}, \mathbf{J}, 0\rangle$ and the non-highest weight states $|\mathbf{I}, \mathbf{J}_0, 1\rangle$. For the highest weight state, a given set of quantum numbers $\{\mathbf{I}_N, \mathbf{J}\}$ determines a unique solution of the BA equations (2), namely, the wave numbers and spin rapidity $\{k_1, k_2, \dots, k_N; \lambda\}$. Then we can have explicit forms of different wave functions. The highest weight state is given by

$$\begin{aligned} |\mathbf{I}, \mathbf{J}, 0\rangle &= \int d\mathbf{x} \Phi_1(\mathbf{x}) \hat{\Psi}_\downarrow^\dagger(x_1) \dots \hat{\Psi}_\uparrow^\dagger(x_N) |0\rangle, \\ \Phi_1(\mathbf{x}) &= \sum_{l=1}^N \frac{1}{\sqrt{N!}} \left[\sum_{\mathcal{P}} (-1)^{\mathcal{P}} e^{i \sum_j x_j k_{\mathcal{P}_j}} \right. \\ &\quad \times \prod_{i < j} [k_{\mathcal{P}_i} - k_{\mathcal{P}_j} + ic \text{sign}(x_j - x_i)] \\ &\quad \left. \times \prod_{j \neq l} \left[\lambda - k_{\mathcal{P}_j} + i \frac{c}{2} \text{sign}(x_l - x_j) \right] \right]. \quad (\text{s13}) \end{aligned}$$

The total spin of this state is $S = S^z = N/2 - 1$. Using the relation Eq. (s12), $|\mathbf{I}, \mathbf{J}_0, 1\rangle = \hat{S}^- |\mathbf{I}, \mathbf{J}_0, 0\rangle$, the non-highest weight states is given by

$$|\mathbf{I}, \mathbf{J}_0, 1\rangle = \sum_{l=1}^N \int dx \Phi_0(x) \times \hat{\Psi}_\uparrow^\dagger(x_1) \dots \hat{\Psi}_\downarrow^\dagger(x_l) \dots \hat{\Psi}_\uparrow^\dagger(x_N) |0\rangle. \quad (\text{s14})$$

The total spin of this state $S = N/2$ and $S^z = N/2 - 1$.

S3.2 Matrix element

Based on the discussions above, we need to calculate A_α and $B_{\alpha,\beta}$ for the time evolution of impurity momentum $K_\downarrow(t)$. Using the specific forms of the wave functions of the relevant states Eqs. (s12-s14), and following the method [4, 5]. we can directly calculate A_α and $B_{\alpha,\beta}$. Explicitly, we have

$$\begin{aligned} A_\alpha &= \frac{\langle \alpha | \Phi_1 \rangle}{\sqrt{\langle \alpha | \langle \Phi_1 \rangle}} = \int dx \frac{\langle \alpha | \phi_\downarrow(x) \Psi_\downarrow^\dagger(x) | \Omega \rangle}{\sqrt{\langle \alpha | \langle \Phi_1 \rangle}} \\ &= \int e^{-iK_\alpha x} dx \phi_\downarrow(x) \frac{\langle \alpha | \Psi_\downarrow^\dagger(0) | \Omega \rangle}{\sqrt{\langle \alpha | \langle \Phi_1 \rangle}}, \end{aligned} \quad (\text{s15})$$

$$\begin{aligned} \langle \Phi_1 \rangle &= \int dy \phi_\downarrow^*(y) \langle \Omega | \hat{\Psi}_\downarrow(y) \int dx \phi_\downarrow(x) \hat{\Psi}_\downarrow^\dagger(x) | \Omega \rangle \\ &= \int dx |\phi_\downarrow(x)|^2 \langle \Omega \rangle. \end{aligned} \quad (\text{s16})$$

We further calculate norms and overlaps, where $|\Omega\rangle = |\mathbf{I}_{N-1}, \mathbf{J}_0, 0\rangle$, $|\alpha\rangle = |\mathbf{I}_N, J, 0\rangle$ or $|\alpha\rangle = \hat{S}^- |\mathbf{I}_N, \mathbf{J}_0, 0\rangle = |\mathbf{I}_N, \mathbf{J}_0, 1\rangle$.

The norm of the state $|\mathbf{I}, \mathbf{J}_0, 0\rangle$ is given by

$$\langle \mathbf{I}_N, \mathbf{J}_0, 0 \rangle = \prod_{i < j} [(k_i - k_j)^2 + c^2] \det(\mathcal{G}), \quad (\text{s17})$$

$$\mathcal{G}_{ij} = \delta_{i,j} \left[L + \sum_{l=1}^N \phi_1(k_i - k_l) \right] - \phi_1(k_i - k_j),$$

$$\phi_n(u) = \frac{2cn}{n^2 u^2 + c^2},$$

where $\{k_1, k_2, \dots, k_N\}$ are the solution of BA equation (2) with the quantum numbers \mathbf{I}_N . The norm of non-highest weight state $|\mathbf{I}, \mathbf{J}_0, 1\rangle$ can also be calculated by using Eq. (s17), namely,

$$\langle \mathbf{I}_N, \mathbf{J}_0, 1 \rangle = \langle \mathbf{I}_N, \mathbf{J}_0, 0 | \hat{S}^+ \hat{S}^- | \mathbf{I}_N, \mathbf{J}_0, 0 \rangle = N \langle \mathbf{I}_N, \mathbf{J}_0, 0 \rangle.$$

Then the norm of the state $|\mathbf{I}, J, 0\rangle$ is given by the following equation

$$\begin{aligned} \langle \mathbf{I}, J, 0 \rangle &= \left| \frac{1}{-ic} \prod_{j=1}^N [\lambda - k_j - ic'] \prod_{i < j} [k_i - k_j + ic] \right|^2 \\ &\times c \det \mathcal{J}, \end{aligned} \quad (\text{s18})$$

where \mathcal{J} is a $N + 1$ -dimensional matrix, explicitly,

$$\begin{aligned} \mathcal{J} &= \begin{pmatrix} J_{kk} & J_{k\lambda} \\ J_{\lambda k} & J_{\lambda\lambda} \end{pmatrix}_{N+1}, \\ (J_{kk})_{ij} &= \delta_{ij} \left[L + \sum_{m=1}^N \phi_1(k_i - k_m) - \phi_2(k_i - \lambda) \right] \\ &\quad - \phi_1(k_i - k_j), \\ (J_{k\lambda})_{i,N+1} &= \phi_2(k_i - \lambda), \quad (J_{\lambda k})_{N+1,j} = -\phi_2(k_j - \lambda), \\ (J_{\lambda\lambda})_{N+1,N+1} &= \sum_{m=1}^N \phi_2(k_m - \lambda), \end{aligned}$$

and $\{k_1, k_2, \dots, k_N; \lambda\}$ are the solution of BA equation (2) with the quantum numbers \mathbf{I}_N and J .

To calculate $\langle \alpha | \Psi_\downarrow^\dagger(0) | \Omega \rangle$ we need the matrix elements $\langle \mathbf{I}'_{N-1}, \mathbf{J}_0, 0 | \hat{\Psi}_\downarrow(0) | \mathbf{I}_N, J, 0 \rangle$ and $\langle \mathbf{I}'_{N-1}, \mathbf{J}_0, 0 | \hat{\Psi}_\downarrow(0) | \mathbf{I}_N, \mathbf{J}_0, 1 \rangle$ for the highest and non-highest weight $|\alpha\rangle$, respectively. The matrix element $\langle \mathbf{I}'_{N-1}, \mathbf{J}_0, 0 | \hat{\Psi}_\downarrow(0) | \mathbf{I}_N, J, 0 \rangle$ is give by

$$\begin{aligned} \langle \mathbf{I}'_{N-1}, \mathbf{J}_0, 0 | \hat{\Psi}_\downarrow(0) | \mathbf{I}_N, J, 0 \rangle &= \sqrt{N} (N-1)! \det \mathcal{M} \\ &\times \frac{\prod_{i > j} (k_i - k_j + ic) \quad -ic}{\prod_{l > m} (q_l - q_m + ic) \prod_j (\lambda - k_j - ic)}. \end{aligned} \quad (\text{s19})$$

Here the $(N-1) \times (N-1)$ matrix \mathcal{M} has elements $\mathcal{M}_{jk} = M_{jk} - M_{N,k}$,

$$\begin{aligned} M_{jk} &= t(q_k - k_j) h_2(\lambda - k_j) \frac{\prod_{m=1}^{N-1} h_1(q_m - k_j)}{\prod_{m=1}^N h_1(k_m - k_j)} \\ &\quad + t(k_j - q_k) h_2(k_j - \lambda) \frac{\prod_{m=1}^{N-1} h_1(k_j - q_m)}{\prod_{m=1}^N h_1(k_j - k_m)}, \\ h_n(u) &= u + i \frac{c}{n}, \quad t(u) = \frac{-c}{u(u + ic)}, \end{aligned}$$

where $\{q_1, q_2, \dots, q_{N-1}\}$ are the solution of the BA equations (2) with the quantum numbers \mathbf{I}_{N-1} .

For the matrix element of the non-highest weight state $|\alpha\rangle$, we have

$$\begin{aligned} \langle \mathbf{I}'_{N-1}, \mathbf{J}_0, 0 | \hat{\Psi}_\downarrow(0) | \mathbf{I}_N, \mathbf{J}_0, 1 \rangle &= \langle \mathbf{I}'_{N-1}, \mathbf{J}_0, 0 | \hat{\Psi}_\downarrow(0) \hat{S}^- | \mathbf{I}_N, \mathbf{J}_0, 0 \rangle \\ &= N \langle \mathbf{I}'_{N-1}, \mathbf{J}_0, 0 | \hat{\Psi}_\uparrow(0) | \mathbf{I}_N, \mathbf{J}_0, 0 \rangle, \end{aligned}$$

where $\langle \mathbf{I}'_{N-1}, \mathbf{J}_0, 0 | \hat{\Psi}_\uparrow(0) | \mathbf{I}_N, \mathbf{J}_0, 0 \rangle$ is the matrix element of the Lieb-Liniger model

$$\begin{aligned} \langle \mathbf{I}'_{N-1}, \mathbf{J}_0, 0 | \hat{\Psi}_\uparrow(0) | \mathbf{I}_N, \mathbf{J}_0, 0 \rangle &= (N-1)! \sqrt{N} \frac{\prod_{i > j} (k_i - k_j + ic)}{\prod_{l > m} (q_l - q_m + ic)} \det \mathcal{S}, \end{aligned} \quad (\text{s20})$$

where $\mathcal{S}_{ij} = S_{i,j} - S_{N,j}$,

$$S_{ij} = t(q_j - k_i) \frac{\prod_{m=1}^{N-1} h_1(q_m - k_i)}{\prod_{m=1}^N h_1(k_m - k_i)}$$

$$-t(k_i - q_j) \frac{\prod_{m=1}^{N-1} h_1(k_i - q_m)}{\prod_{m=1}^N h_1(k_i - k_m)},$$

$$h_n(u) = u + i\frac{c}{n}, \quad t(u) = \frac{-c}{u(u+ic)}.$$

The above determinant forms are convenient for us to perform numerical calculations.

In order to calculate $B_{\alpha,\beta}$

$$B_{\alpha\beta} = \frac{\langle \beta | \hat{\Psi}_\downarrow(0) | \alpha \rangle}{\sqrt{\langle \alpha | \alpha \rangle \langle \beta | \beta \rangle}}, \quad (\text{s21})$$

we need to calculate norms $\langle \alpha |$, $\langle \beta |$ and the overlap $\langle \beta | \hat{\Psi}_\downarrow(0) | \alpha \rangle$. Where $|\beta\rangle = |\mathbf{I}'_{N-1}, \mathbf{J}_0, 0\rangle$ and is the Bethe state of $N-1$ particles with all spin up. Similar to the calculation of A_α , here $|\alpha\rangle$ also involves the highest or non-highest weight states, namely, $|\alpha\rangle = |\mathbf{I}_N, J, 0\rangle$ and $|\alpha\rangle = |\mathbf{I}_N, \mathbf{J}_0, 1\rangle$, respectively. The norms can be calculated by Eqs. (s17, s18). Similarly, for the highest weight state $|\alpha\rangle$ we can calculate the matrix element by using Eq. (s19)

$$\langle \beta | \hat{\Psi}_\downarrow(0) | \alpha \rangle = \langle \mathbf{I}'_{N-1}, \mathbf{J}_0, 0 | \hat{\Psi}_\downarrow(0) | \mathbf{I}_N, J, 0 \rangle.$$

When $|\alpha\rangle$ is the non-highest weight state

$$\begin{aligned} \langle \beta | \hat{\Psi}_\downarrow(0) | \alpha \rangle &= \langle \mathbf{I}'_{N-1}, \mathbf{J}_0, 0 | \hat{\Psi}_\downarrow(0) \hat{S}^- | \mathbf{I}_N, \mathbf{J}_0, 0 \rangle \\ &= N \langle \mathbf{I}'_{N-1}, \mathbf{J}_0, 0 | \hat{\Psi}_\uparrow(0) | \mathbf{I}_N, \mathbf{J}_0, 0 \rangle, \end{aligned}$$

which is given by Eq. (s20).

S3.3 Magnon- and exciton-like states

Quasiparticles are used to describe individual or collective excitations. Taking the magnon as an example, its appearance is due to the transmission of spin wave in a ferromagnetic state. The essence of excitation is a change in quantum numbers in Bethe ansatz. It describes quasi-particles in this way. Using the ground state as a reference, $-N/2 < \mathbf{I} < N/2$. One type of excited states which is formed after impurity enters the system is worth noting. As shown in (a) of FIG. 2 [as mentioned in the main text], the red states have a complete Fermi Sea (without hole inside), plus an external particle I_p . The quantum number J indicates that the system undergoes a spin flip and propagates at a certain speed. The excitation energy is $E \approx \frac{2\pi^2}{3\gamma m} q^2$ for a strong interaction, showing a magnon-like state. Here q is the total momentum of the system.

In contrast, for the exciton states (with one hole in the “Fermi sea”), their J s of the blue states in Fig. 2 in the main text is close to $-N/2$, resulting in a spin excitation energy is about 0. We will further demonstrate in the following Section 4, a particle at the left Fermi point coupled to a deep hole in Fermi sea form the exciton

state. This situation is much like an exciton, where an electron in the conduction band is bound to a hole in the valence band. Therefore we call the blue states in Fig. 2 in the main text as exciton-like states. After quenching, the system undergoes dynamic evolution through energy transfer between different states.

For an impurity with variation of the mass and the initial momentum, the quenching dynamics results in the excitation of particle-hole pairs, where the single particle-hole pairs are the primary contributors. The closer the hole is to the Fermi surface, the higher the weight of the state is [11–15], where the impurity initial velocity is not larger than the sound velocity of the medium. In the papers [11–14], authors gave insightful understanding of the long time evolution from the particle-hole excitations. In the long time limit, diagonal ensemble plays an important role so that the overlaps between the initial state and the excited states are the key ingredient for their study of the dynamics of the impurity of the impurity model. However, for a supersonic impurity, this case is not the full features of the impurity dynamics.

Here we use quantum numbers \mathbf{I} to classify the highest weight states. In principle, all the possible choices of quantum numbers satisfy the restrictions of Eq. (2) [as mentioned in the main text] and the selection rules above should be taken account. Here we only classify the states where \mathbf{I} have a clear structure of “Fermi sea”, there is no hole or only one hole I_h inside the “Fermi sea” and only one particle I_p outside the “Fermi sea”.

The magnon- and exciton-like states essentially comprise the feature of QF and quantum revival phenomena, see FIG.2 in the main text. The dots and arrows denote quantum numbers \mathbf{I} and J , respectively. We regard the state without hole inside the “Fermi sea” as magnon-like state, FIG. s1 (a), while the state with only one hole in the deep Fermi sea as exciton-like state, FIG. s1 (b). The \mathbf{I} of magnon- and exciton-like states have the following form

$$\begin{aligned} \mathbf{I}^m &= \{I_0^m, I_1^m, \dots, I_{N-2}^m, I_p^m\}, \\ \mathbf{I}^e &= \{I_0^e, I_1^e, \dots, I_{h-1}^e, I_{h+1}^e, \dots, I_{N-1}^e, I_p^e\}, \end{aligned} \quad (\text{s22})$$

respectively. We denote the quantum number of spin-down particle as J^m and J^e for magnon- and exciton-like states, respectively. Here, I_ℓ are the quantum numbers in the “Fermi sea”, $I_\ell = I_0 + \ell$, I_0 is the starting quantum number of the “Fermi sea”, $\ell = 1, 2, \dots, N-1$, I_p is the quantum number of particle excitation and I_h is location of hole in the exciton-like states. Note that the quantum number J is fixed for a given \mathbf{I} of the emitted particle when the impurity is injected with a large momentum Q into the medium of the Lieb-Liniger Bose gas. This is mainly because of the conservation of momentum¹. We denote

¹ In the TABLE s1, the sum rule of magnons (excitons) also involves the magnons with other I_0^m (I_0^e).

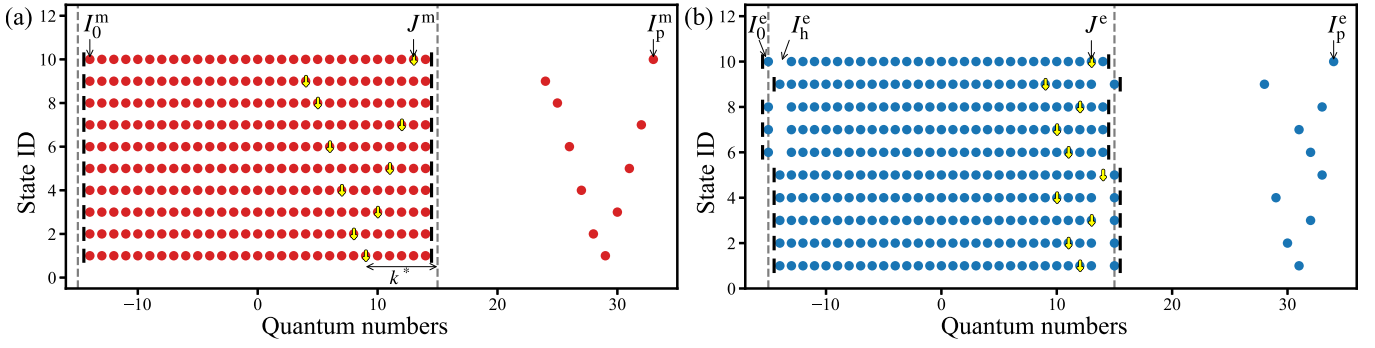


FIG. s1. Quantum numbers of magnon-like states (a) and exciton-like states (b). The dots and yellow arrows are quantum numbers I and J , respectively. The short thick straight lines show the clear “Fermi surfaces” structure of I . The thin black dashed straight lines are the Fermi points of the system where $I = \pm N/2$. We select the top 10 states with largest $|A|^2$ of magnon- and particle-hole excitation states and plot them in (a) and (b), respectively. When the hole in (b) locates in deep “Fermi sea”, we name the state as exciton-like in the paper. Here $\gamma = 10$, $Q = 1.33k_F$ and $N = 30$.

TABLE s1. Values of sum rule $\sum |A_\alpha|^2$ and state numbers in our numerical calculations. The values outside of brackets are $\sum |A_\alpha|^2$ and the values inside of brackets are numbers of states taken account in our calculations. Here, $N = 30$ and $\gamma = 10$.

Q	total	magnon	exciton	other HS ^{*1}	NHS ^{*2}
$1.33k_F$	0.97(86795)	0.711	0.040	0.192	0.025
$1.07k_F$	0.96(89928)	0.696	0.041	0.193	0.030
$1.00k_F$	0.95(90682)	0.691	0.041	0.187	0.031
$0.80k_F$	0.95(92817)	0.673	0.043	0.201	0.033
$0.53k_F$	0.95(95190)	0.641	0.047	0.223	0.039
$0.13k_F$	0.95(97221)	0.539	0.074	0.263	0.074

(*1), other HS: other highest weight states;

(*2), NHS: non-highest weight states.

the most important quantum numbers in the study of the QF and quantum revival phenomena, namely,

$$\begin{aligned} \text{magnon-like states: } & \{I_p^m, J^m\}, \\ \text{exciton-like states: } & \{I_p^e, I_h^e, J^e\}. \end{aligned} \quad (\text{s23})$$

Now we have all ingredients to calculate precisely $K_\downarrow(t)$ to capture the essence of the dynamics of the QF and quantum revival. Without losing generality, we in this paper take the impurity wave packet as a plane wave. Precisely speaking, we also treat the sum rule $\sum |A_\alpha|^2$ larger than 95% in our actual calculations, see TABLE. s1. As shown in TABLE. s1, the magnon-like states have the largest $\sum |A_\alpha|^2$ and they are the most important states in the supersonic impurity phenomenon. The sum rule of exciton-like states are relatively small. We will show the importance of these states in the QF phenomenon in Sec. S4 in this supplemental material. The states other than the mentioned highest weight states and the non-highest weight states are all necessary in the calculation of $K_\downarrow(t)$. Although they make very small

contributions to the dynamics of the QF and quantum revival, our calculations show that if the contribution of these states is ignored, the results will have obvious difference (about 5 percent), indicating that these states have non-trivial contribution.

The sum rule of the matrix element $B_{\alpha\beta}$ depends on α , see Eqs.(s10). Based on the sum rule of weights, we observe that the magnon-like states are of the most importance in the matrix element $B_{\alpha\beta}$. We denote N_{AMS} as the number of accounted magnon-like states (AMS) in our numerical calculations. In this paper, we request the numerical sum rule $L \sum_{\alpha \in \text{AMS}} \sum_{\beta} |B_{\alpha\beta}|^2 > 0.97N_{\text{AMS}}$.

S3.4 Exciton energy in the thermodynamic limit

In this section, we discuss the excitation energies of magnon- and exciton-like states in the thermodynamic limit. Building on the BA solution in the thermodynamic limit, i.e., $N \rightarrow \infty$, $L \rightarrow \infty$ and $\gamma = cL/N$ is finite. The energy of excited states is calculated by using the thermodynamic Bethe ansatz (TBA) equations [3, 6, 7]. The medium $|\Omega\rangle$ is the ground state of the Lieb-Liniger gas and the TBA equations of this model is given in [8–10], namely,

$$\begin{aligned} \rho_c(k) + \rho_c^h(k) &= \frac{1}{2\pi} + \int_{-k_0}^{k_0} a_2(k-k')\rho^c(k')dk', \\ \varepsilon_c(k) &= k^2 - \mu + \int_{-k_0}^{k_0} a_2(k-k')\varepsilon_c(k')dk', \end{aligned} \quad (\text{s24})$$

where $\rho_c(k)$ is the linear density,

$$\rho_c(k) = \begin{cases} \rho_c(k), & |k| < k_0, \\ 0, & |k| > k_0, \end{cases} \quad \rho_c^h(k) = \begin{cases} 0, & |k| < k_0, \\ \rho_c^h(k), & |k| > k_0, \end{cases}$$

$\varepsilon_c(k)$ is the dressed energy of the charge sector and the integral kernel $a_n(x) = nc/[2\pi(x^2 + n^2c^2)]$. Here, k_0 is

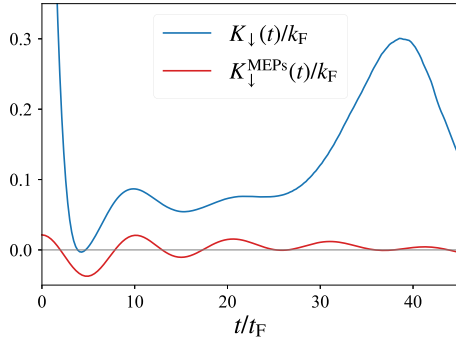


FIG. s2. The time evolution of impurity momentum $K_{\downarrow}(t)$ when $\gamma = 10$, $Q = 1.33k_{\text{F}}$ and $N = 30$. The blue line is calculated with all of the states in TABLE. s1 and the red line is calculated by the special MEPS in Eq. (s30).

the Fermi point (cut-off) of the wave numbers k and it is determined by $\int_{-k_0}^{k_0} \rho(k)dk = N/L$. μ is the chemical potential and it is determined by the condition $\varepsilon_c(k_0) = 0$. The TBA equations for the density and dressed energy of the spin degree of freedom are given by

$$\begin{aligned} \rho_s(\lambda) + \rho_s^h(\lambda) &= \int_{-k_0}^{k_0} a_1(k - \lambda) \rho_c(k) dk, \\ \varepsilon_s(\lambda) &= - \int_{-k_0}^{k_0} a_1(k - \lambda) \varepsilon_c(k) dk, \end{aligned} \quad (\text{s25})$$

respectively.

The starting quantum number I_0 of the magnon- and exciton-like states in Eqs. (s23) are near by the left Fermi point, $\lim_{L \rightarrow \infty} 2\pi I_0/L = -k_{\text{F}}$, where the Fermi momentum $k_{\text{F}} = \pi N/L$. The excitation energies carried by the quantum numbers near by the Fermi surface are zero. The excitation energies of magnon-like and exciton-like states associated with the quantum numbers Eqs. (s23) can be expressed as [6, 9]

$$\begin{aligned} \Delta E_{\text{m}} &= \mu + \varepsilon_c(k_{\text{p}}^{\text{m}}) + \varepsilon_s(\lambda^{\text{m}}), \\ \Delta E_{\text{e}} &= \mu + \varepsilon_c(k_{\text{p}}^{\text{e}}) - \varepsilon_c(k_{\text{h}}^{\text{e}}) + \varepsilon_s(\lambda^{\text{e}}), \end{aligned} \quad (\text{s26})$$

respectively. Here, $k_{\text{p}}^{\text{m,e}}$, k_{h}^{e} and $\lambda^{\text{m,e}}$ are the rapidities of the corresponding quantum numbers $I_{\text{p}}^{\text{m,e}}$, I_{h}^{e} and $J^{\text{m,e}}$, respectively. They can be determined by the following equations

$$\begin{aligned} \frac{I}{L} &= \int_0^k [\rho_c(k') + \rho_c^h(k')] dk', \\ \frac{J}{L} &= \int_0^\lambda [\rho_s(\lambda') + \rho_s^h(\lambda')] d\lambda'. \end{aligned} \quad (\text{s27})$$

S4. QUANTUM FLUTTER

We presented the expression of the impurity momentum $K_{\downarrow}(t)$ in Sec. S2. Using the determinant formula of

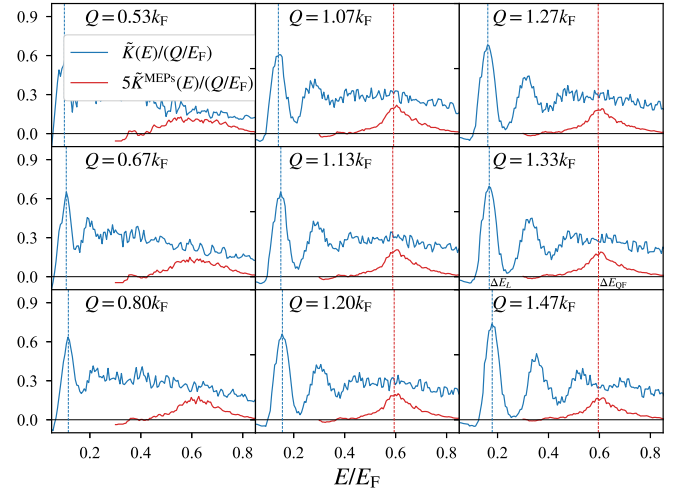


FIG. s3. The impurity momentum $\tilde{K}_{\downarrow}(E)$ in frequency space for different initial impurity momentum Q and a fixed interaction strength $\gamma = 10$. The blue lines show $\tilde{K}_{\downarrow}(E)$ in frequency space by means of the Eq. (s29). The vertical blue lines indicates the revival frequency determined by the magnon pairs with different values of the Q , see Sec. S5. It is near the frequency $0.15E_{\text{F}}$, the typical energy of quantum revivals, ΔE_L . The vertical red dashed lines nearby $0.6E_{\text{F}}$ gives the typical frequency of the QF, i.e. ΔE_{QF} . In the calculation of $\tilde{K}_{\downarrow}(E)$ via Eq. (s29) we set $N = 30$ and $\Delta E = 0.03E_{\text{F}}$. While the red lines are 5 times of the actual value.

the norms, overlap and matrix element obtained in the Sec. S3, we presented the impurity momentum $K_{\downarrow}(t)$ and momentum distributions in the main text. In order to conceive the microscopic origin of QF, we first study the frequency (energy) spectrum of $K_{\downarrow}(t)$

$$\tilde{K}_{\downarrow}(E) = \frac{1}{2\pi} \int dt e^{-iEt} K_{\downarrow}(t). \quad (\text{s28})$$

In Eqs. (s9), $K_{\alpha\alpha'}$ is the momentum matrix element of the state pair $\{|\alpha\rangle, |\alpha'\rangle\}$ and it has close relation with frequency spectrum $\tilde{K}_{\downarrow}(E)$ Eq. (s28). We can calculate $\tilde{K}_{\downarrow}(E)$ by taking the average value of $K_{\alpha\alpha'}$ in a small energy interval

$$\tilde{K}_{\downarrow}(E) = \frac{L}{2\Delta E} \sum_{\alpha\alpha'}^{\Delta E} K_{\alpha\alpha'}, \quad (\text{s29})$$

where $K_{\alpha\alpha'}$ is given by Eq. (s9). In the above equation, $\Delta E \ll E_{\text{F}}$ and $E - \Delta E < E_{\alpha} - E_{\alpha'} < E + \Delta E$, and the summation $\Sigma^{\Delta E}$ is taken over all of the state pairs.

As being given in Eq. (s28), $\tilde{K}_{\downarrow}(E)$ is the oscillation amplitude of $K_{\downarrow}(t)$ at the frequency (energy) E . We observe that the state pairs $\{|\alpha\rangle, |\alpha'\rangle\}$ with an energy difference $E \sim E_{\alpha} - E_{\alpha'}$ essentially attribute to the oscillation nature of the impurity momentum $\tilde{K}_{\downarrow}(E)$, see Eq. (s29). $\tilde{K}_{\downarrow}(E)$ is plotted in FIG. s3 in which several peaks were observed. The first peak of $\tilde{K}_{\downarrow}(E)$ reveals the

typical energy of quantum revival, which is governed by the magnon pairs with nearest neighbour quantum numbers I_p^m . The second peak is from the magnon pairs with next nearest neighbour I_p^m , and so on. We will discuss about the revival dynamics later. The numerical result of $\tilde{K}_\downarrow(E)$ shows that the typical energy of QF ΔE_{QF} , is nearby $0.6E_F$ for the system with $\gamma = 10$. This strikingly indicates that the frequency of the QF does not dependent on the initial momentum of the impurity once it is over the intrinsic sound velocity of the medium. We also observed from $\tilde{K}_\downarrow(E)$ that the QF information of $\tilde{K}_\downarrow(E)$ is concealed by the peaks of magnon pairs, see FIG. s3.

So far, we realize that magnon pairs do not really contribute the frequency of the QF. Such an oscillation feature of QF is essentially resulted in from the magnon-exciton pairs (MEPs) described by the quantum numbers Eqs. (s23). We observe that the quantum number I_p in the two states of one MEP are the same, presenting an emitted particle. Based on the conservation of the momentum, we only need to consider the quantum numbers of hole in the exciton and spin-down quantum number in magnon state

$$\{I_h^e, J^m\}. \quad (\text{s30})$$

The other quantum numbers can be given by I_h^e, J^m , namely, $I_p^m = QL/2\pi + J^m$ and $J^e = I_p^e - QL/2\pi - N/2 - I_h^e = J^m - N/2 - I_h^e$. We take the summation in Eq. (s29) over the selected MEPs in Eq. (s30) and denote it as $\tilde{K}_\downarrow^{\text{MEPs}}(E)$. We plot $\tilde{K}_\downarrow^{\text{MEPs}}(E)$ (red lines) in FIG. s3. It is clear seen that the QF oscillations of $K_\downarrow(t)$ and the QF peaks of $\tilde{K}_\downarrow(E \sim \Delta E_{\text{QF}})$ originate from the coherent dynamics of the MEPs.

In order to deeply understand the microscopic origin of the QF, we try to find the most relevant MEPs that comprise the characteristic of the QF. In the FIG. 2 in the main text, we consider the case when $N = 30$ and $\gamma = 10$. Further analysis shows that the MEP with quantum number $\{I_h^e, J^m\} = \{-1, 1\}$ is the most relevant one. In FIG. s3, we plot $\tilde{K}_\downarrow^{\text{MEPs}}(\Delta E_{\text{QF}})$ with the characteristic energy difference ΔE_{QF} between the pair states ΔE_{QF} . In the thermodynamic limit, we observe that $k_p^m = k_p^e$ because of $I_p^m = I_p^e$. Thus Eqs. (s26) gives

$$\Delta E_{\text{QF}} = |\varepsilon_c(k_h^e) - \varepsilon_s(\lambda^e) + \varepsilon_s(\lambda^m)|. \quad (\text{s31})$$

In the thermodynamic limit, we further find from the TBA equations that $k_h^e = 0$, $\lambda^m = 0$ and $\lambda^e = -\infty$. Consequently the oscillation frequency (energy) of the QF is given by

$$\Delta E_{\text{QF}} = |\varepsilon_c(0)| - |\varepsilon_s(0)|. \quad (\text{s32})$$

Here $\varepsilon_c(0) < 0$, $\varepsilon_s(0) > 0$ and $\varepsilon_s(\pm\infty) = 0$. It follows that the result of Eq. (6) periodicity of QF in the main text

$$\tau_{\text{QF}} = \frac{2\pi}{|\varepsilon_c(0)| - |\varepsilon_s(0)|}. \quad (\text{s33})$$

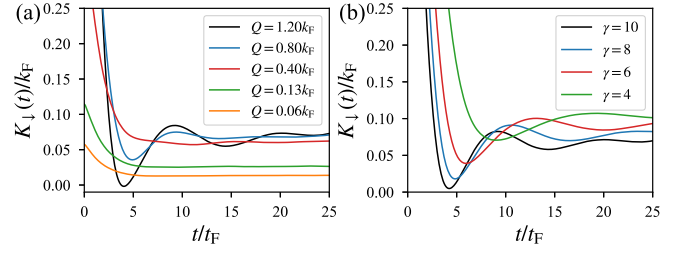


FIG. s4. QF of different conditions when $N = 30$. (a), $K_\downarrow(t)$ when $\gamma = 10$ for different injected momentum Q . (b), QF for different interaction strength γ when $N = 30$ when $Q = 1.07k_F$.

For the strong coupling limit we have $|\varepsilon_c(0)| - |\varepsilon_s(0)| = E_F[1 - 20\gamma/3 + \mathcal{O}(\gamma^{-2})]$ that gives

$$\tau_{\text{QF}} = 2\pi t_F \left[1 + \frac{20}{3\gamma} + \mathcal{O}(\gamma^{-2}) \right]. \quad (\text{s34})$$

These results were confirmed in the FIG.3 in the main text.

In FIG. s4 (a), we further demonstrate the dynamics of impurity momentum for different initial momenta, ranging from $Q < k_F$ to $Q > k_F$. It is showed that the saturated momentum approximately approaches to the same value, but the oscillation amplitude increases when the Q becomes larger. When Q is small, the QF no longer appears and the saturated momentum gradually turns to zero as decreasing the Q . In view of the fast decay process of $K_\downarrow(t)$, we observe that the momentum of the impurity decays faster when Q becomes larger. When Q is large, K_\downarrow even reach a negative value after the faster decay. When the impurity is injected into the medium, the density of the medium in front of the faster moving impurity increases quickly so that quantum friction between the impurity and medium increases quickly. When the initial momentum Q is larger than a critical value, the density of the medium in front of the impurity can be so dense such that the impurity rebounds back from it. In FIG. s4 (b), we demonstrate the interaction effect in the faster decay process and the oscillation period. From the QF periodicity Eq. (6) in the main text, we observe that the periodicity τ_{QF} increases wen the interaction γ decreases, see FIG. 3 in the main text.

S5. QUANTUM REVIVAL

Now we proceed to discover a microscopic origin of the quantum revival from both $K_\downarrow(t)$ and $\tilde{K}_\downarrow(E)$. The first peak of $\tilde{K}_\downarrow(E)$ in FIG. s3 shows that the frequency is the energy difference between the states in a magnon pair with nearest sequency quantum number I_p^m , see our discussion to the beginning of Sec. S3. Similar to the analysis on the QF, here we further show that the first

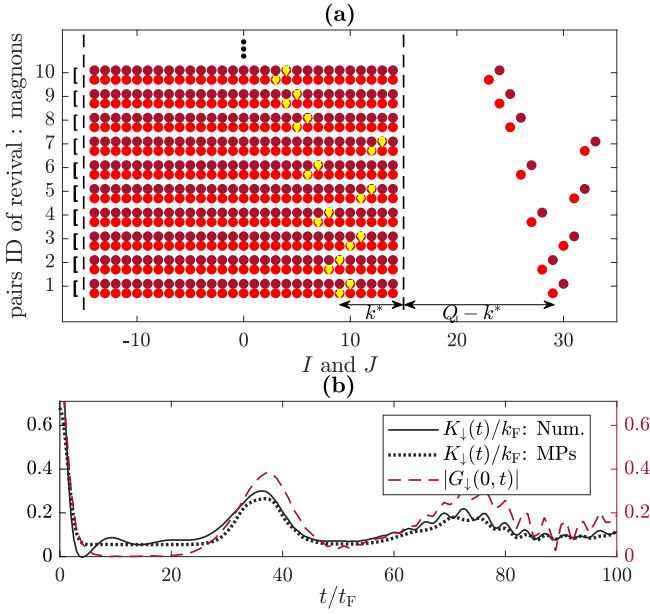


FIG. s5. The large weight pairs for quantum revival dynamics. (a) The red dots stand for the quantum numbers of charges I . Whereas the yellow arrows \downarrow indicates the quantum number J . The orders of these projected states are the magnon states with large values of sum rule weights $|A_\alpha|^2 + |A_{\alpha'}|^2$ used in Eq. (4) in the main text. The positions of the down spins in the pair are adjacent. Here we present the top 10 of such pairs of magnon-like projected states. We define the distance of the quantum number J to the Fermi surface as k^* . (b) The quantum revival of $K_\downarrow(t)$ is obtained from the numerical result (black solid line) and from the propagator (red dashed line) for a plane wave impurity, showing a good agreement with the result (the black dotted line) obtained from the states of MPs in (a). Here the particle number $N = 30$, interaction strength $\gamma = 10$ and the initial momentum $Q = 1.33k_F$.

magnon pair illustrated in FIG. s1 (a) determines the position of the first peak of the $\bar{K}_\downarrow(E)$. This is the most prominent pair of the magnon-like states for the dynamics of the quantum revival. Such a pair of the magnon-like states show the largest weight of $|A_\alpha|^2$, see FIG. s1 (a) and FIG. s5.

The magnon-like states are denoted by $\{I_p^m, J^m\}$ in Eqs. (s23). We denote the quantum numbers of the two states in the most prominent pair as $\{I_1, J_1\}$ and $\{I_2, J_2\}$, respectively, leading to the largest weight $|A_\alpha|^2$. More precisely,

$$I_2 = I_1 \pm \Delta I, \quad J_2 = J_1 \pm \Delta J, \quad (\text{s35})$$

following which we have

$$k_2 = k_1 \pm \Delta k, \quad \lambda_2 = \lambda_1 \pm \Delta \lambda, \quad (\text{s36})$$

namely $\Delta I = \Delta J = 1$, where the $k_{1,2}$ ($\lambda_{1,2}$) here are the corresponding wave numbers (rapidity) of $I_{1,2}$ ($J_{1,2}$).

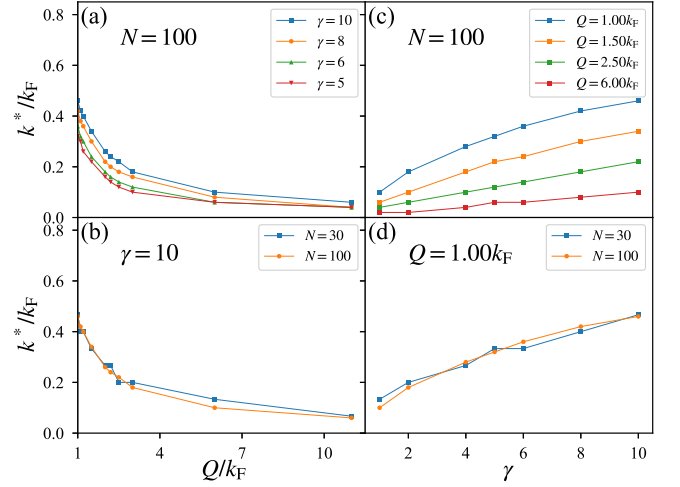


FIG. s6. Numerical determination of the parameter k^* . (a) The parameter k^* v.s. the initial impurity momentum shows the dependence of the interaction. (b) The parameter k^* v.s. the initial impurity momentum shows the independence of the total particle number. (c) The parameter k^* v.s. the interaction strength shows the dependence of the initial momentum Q . (d) The parameter k^* v.s. the interaction strength shows the independence of the total partial number.

The energy difference of the two states in this prominent pair gives the quantum revival ΔE_L . From Eq. (s26), we have

$$\begin{aligned} \Delta E_L &= \lim_{L \rightarrow \infty} |\varepsilon_c(k_2) - \varepsilon_c(k_1) + \varepsilon_s(\lambda_2) - \varepsilon_s(\lambda_1)| \\ &= \lim_{L \rightarrow \infty} |\Delta k \varepsilon'_c(k_1) + \Delta \lambda \varepsilon'_s(\lambda_1)| \\ &= \lim_{L \rightarrow \infty} \left| \frac{\Delta k}{\Delta I} \Delta I \varepsilon'_c(k_1) + \frac{\Delta \lambda}{\Delta J} \Delta J \varepsilon'_s(\lambda_1) \right|. \end{aligned} \quad (\text{s37})$$

Moreover, we define

$$\begin{aligned} \lim_{L \rightarrow \infty} \frac{\Delta I}{L \Delta k} &= \rho_c(k) + \rho_c^h(k), \\ \lim_{L \rightarrow \infty} \frac{\Delta J}{L \Delta \lambda} \Delta J &= \rho_s(k) + \rho_s^h(k). \end{aligned} \quad (\text{s38})$$

Then the characteristic energy of quantum revival can be given by

$$\Delta E_L = \Delta p |v_p(Q - k^*) - v_s(k^*)|, \quad (\text{s39})$$

with $k^* = k_F - \frac{2\pi}{L} J_1$. Here $\Delta p = 2\pi/L$ and sound velocities

$$\begin{aligned} v_p(p) \Big|_{p=(\frac{2\pi}{L} I_1 - k_F)} &= \frac{\varepsilon'_c(k_1)}{2\pi[\rho_c(k_1) + \rho_c^h(k_1)]}, \\ v_s(p) \Big|_{p=(k_F - \frac{2\pi}{L} J_1)} &= \frac{\varepsilon'_s(\lambda_1)}{2\pi[\rho_s(\lambda_1) + \rho_s^h(\lambda_1)]}. \end{aligned}$$

Consequently, we find

$$\Delta E_L = \frac{2\pi}{L} |v_p(Q - k^*) - v_s(k^*)|$$

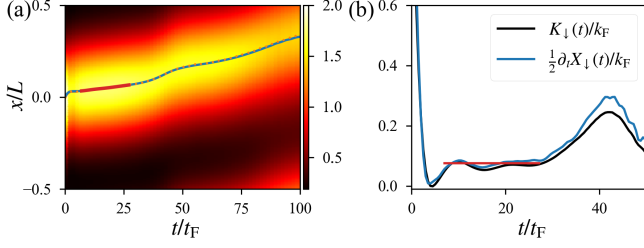


FIG. s7. QF and quantum revival in the injected Gaussian wave packet impurity. (a), The snaking signature occurs in the evolution of the density distribution $\langle \hat{\Psi}_\downarrow^\dagger(x, t) \hat{\Psi}_\downarrow(x, t) \rangle$. The blue line shows the motion of the mass center, $X_\downarrow(t)$, while the orange dots are the motion of wave packet center (position with maximum density). (b) The evolution of impurity momentum (black line) coincides with the evolution of the wave packet center which is defined by $K_\downarrow(t) = \frac{1}{2} \partial_t X_\downarrow(t)$. In a time interval $7t_F < t < 27t_F$, the average momentum (speed) of the mass center is showed by the red straight line, which matches the saturated momentum k_s of the QF flutter. In this figure, we set $\gamma = 10$, $Q = 1.2k_F$ and $a_0 = 0.21L$.

$$= \frac{2\pi}{L} (v_p(Q - k^*) - v_s(k^*)), \quad (\text{s40})$$

where $v_p(p)$ is always larger than $v_s(p)$. This remarkably gives the period of quantum revival Eq. (7) in the main text, namely $\tau_L = 2\pi/\Delta E_L$,

$$\tau_L = \frac{N}{[v_c(Q - k^*) - v_s(k^*)]n} = \frac{L}{v_c(Q - k^*) - v_s(k^*)}. \quad (\text{s41})$$

In this paper, k^* was calculated numerically based on the BA equations. We also observe that k^* is subject to the impurity initial momentum Q and interaction strength γ , see FIG. s6. However, k^* dose not change obviously with respect to N . The revival dynamics of the supersonic impurity reveals the reflection of the collective excitations with respect to the finite-size effect.

S6. SUPERSONIC IMPURITY WITH A GAUSSIAN WAVE PACKET

Now we consider a more realistic supersonic impurity with a Gaussian wave packet injected into the medium of bosonic liquid. The impurity wave packet is given by

$$\phi_\downarrow(x) = e^{iQx} e^{-(x/a_0)^2/2}, \quad (\text{s42})$$

where a_0 is the width of the wave packet. With the help of this injected wave packet, we calculate the evolution of the density distribution of spin-down impurity, namely $\langle \Psi_\downarrow^\dagger(x, t) \Psi_\downarrow(x, t) \rangle$, giving the result showed in FIG. s7 (a). The blue line in FIG. s7 (a) is the mass center of the impurity, showing a novel feature of quantum snaking behavior. More interesting to see that the snaking periodicity is the same as the quantum revival period τ_L . We

also observe that the oscillation dynamics of the QF flutter of the impurity momentum also solely appears only for $Q \gtrsim k_F$, see the black line FIG. s7 (b). The microscopic origin of the QF and quantum revival here are the same as what we have found in the case with a plane wave injected into the bosonic medium.

In fact, the impurity momentum can be measured from the motion of the mass center of the impurity

$$X_\downarrow(t) = \frac{\langle \Phi_I | \hat{x}(t) | \Phi_I \rangle}{\langle \Phi_I \rangle}, \quad (\text{s43})$$

where $\hat{x}(t) = e^{i\hat{H}t} \hat{x} e^{-i\hat{H}t}$ and \hat{x} is the coordinate operator of the impurity. Then

$$\begin{aligned} \partial_t X_\downarrow(t) &= \frac{\langle \Phi_I | e^{i\hat{H}t} [\hat{H}\hat{x} - \hat{x}\hat{H}] e^{-i\hat{H}t} | \Phi_I \rangle}{\langle \Phi_I \rangle} \\ &= \frac{\langle \Phi_I | e^{i\hat{H}t} i[\hat{p}^2 \hat{x} - \hat{x} \hat{p}^2] e^{-i\hat{H}t} | \Phi_I \rangle}{\langle \Phi_I \rangle}, \end{aligned}$$

where \hat{p} is the momentum operator of the impurity. As such, we have that $\hat{x}\hat{p}^2 = \hat{p}^2\hat{x} + 2i\hbar\hat{p}$. It follows

$$\partial_t X_\downarrow(t) = 2\hbar \frac{\langle \Phi_I | \hat{K}_\downarrow(t) | \Phi_I \rangle}{\langle \Phi_I \rangle} = 2\hbar K_\downarrow(t).$$

As mentioned in the main text, we set $\hbar = 1$ here, and then

$$\frac{1}{2} \partial_t X_\downarrow(t) = K_\downarrow(t). \quad (\text{s44})$$

We plot the $\frac{1}{2} \partial_t X_\downarrow(t)$ (blue line) in FIG. s7 (b). The motion of the mass center of the impurity $\frac{1}{2} \partial_t X_\downarrow(t)$ surprisingly coincides with the evolution of the impurity momentum $K_\downarrow(t)$. A slight discrepancy between them is mainly because of the finite size effect. In addition, the sum rules in numerical calculations of $K_\downarrow(t)$ was not taken up to 100%. Therefore, in a realistic experiment, the QF and quantum revival behaviors can be observed by using the motion of the mass center $X_\downarrow(t)$. Where we also plot the saturated momentum of QF as the red line in FIG. (s7) (b).

* jiangyuzhu@wipm.ac.cn
† hqlin@zju.edu.cn
‡ xiwen.guan@anu.edu.au

- [1] C. N. Yang, Phys. Rev. Lett. **19**, 1312 (1967).
- [2] B. Sutherland, Phys. Rev. Lett. **20**, 98 (1968).
- [3] Shi-Jian Gu, You-Quan Li, Zu-Jian Ying and Xue-An Zhao, I. J. Mod. Phys. B **16**, 2137 (2002).
- [4] B. Pozsgay, W.-V. v. G. Oei, and M. Kormos, J. Phys. A: Math. Theor **45**, 465007 (2012).
- [5] R. van den Berg, B. Wouters, S. Eliëns, J. De Nardis, R. M. Konik, and J.-S. Caux, Phys. Rev. Lett. **116**, 225302 (2016).

- [6] Y.-Q. Li, S.-J. Gu, Z.-J. Ying, U. Eckern, EuroPhys. Lett. **61**, 368 (2003).
- [7] X.-W. Guan, M. T. Batchelor and M. Takahashi, Phys. Rev. A **76**, 043617 (2007).
- [8] E. H. Lieb and W. Liniger, Phys. Rev. **130**, 1605 (1963).
- [9] Y. Jiang, Y.-Y. Chen, and X.-W. Guan, Chinese Phys. B **24**, 050311 (2015).
- [10] C. N. Yang, and C. P. Yang, J. Math. Phys. **10**, 1115 (1969).
- [11] E. Burovski, V. Cheianov, O. Gamayun, and O. Lychkovskiy, Phys. Rev. A **89**, 041601(R) (2014).
- [12] O. Gamayun, O. Lychkovskiy, E. Burovski, M. Malcomson, V. V. Cheianov, and M. B. Zvonarev, Phys. Rev. Lett. **120**, 220605 (2018).
- [13] O. Gamayun, O. Lychkovskiy, and M. B. Zvonarev, SciPost. Phys. **8**, 053 (2020).
- [14] O. Gamayun, O. Lychkovskiy, and J.-S. Caux, SciPost. Phys. **8**, 036 (2020).
- [15] O. Gamayun, M. Panfil, F. T. Sant'Ana, Phys. Rev. Res. **5**, 043265 (2023).